Department of Precision and Microsystems Engineering

# Designing Tailored Torque-Twist curves using Variable rate of twist Helicoidal shells

Tomas Zijm

Report no : 2025.071
Coach : Dr. Ir. Giuseppe Radaelli
Professor : Dr. Ir. Giuseppe Radaelli
Specialisation : MNE,MSD
Type of report : Master's Thesis
Date : 26-11-2025

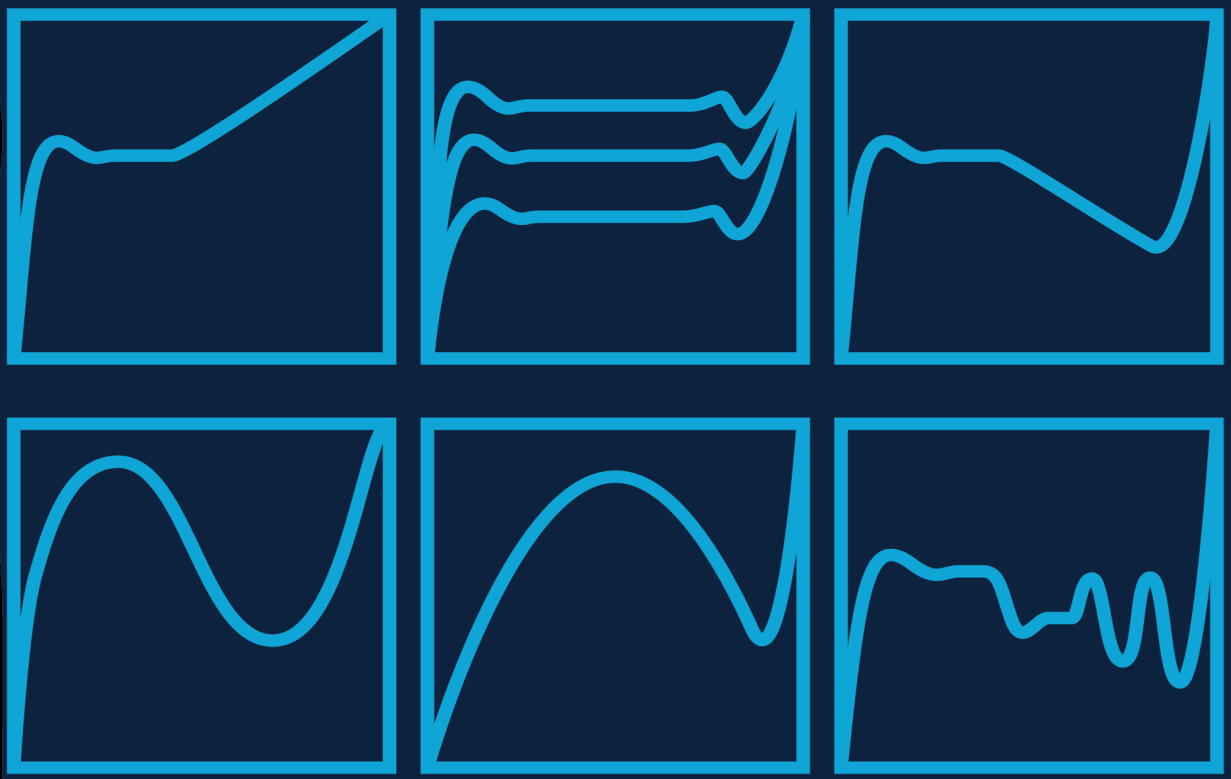

TU Delft Delft University of Technology

Challenge the future


**Delft University of Technology**

Faculty of Mechanical Engineering

The Department of Precision andMicrosystems Engineering (PME)

# Thesis Title

Designing Tailored Torque-Twist curves using Variable rate of twist Helicoidal shells

**M.Sc. Thesis Report**
for ME-HTE MSc Thesis (ME56035)

**Author:**
Tomas Zijm
*M.Sc. Mechanical Engineering*
*(High-tech Engineering Track)*

**Supervisor:**

Dr. Ir. Giuseppe Radaelli

# Preface

The following work is the master's thesis "Designing Tailored Torque-Twist curves using Variable rate of twist Helicoidal shells" written during my master's HighTech engineering at the Delft University of Technology. The main paper describes a design method that allows for the creation of multi-region tailored torque-twist curves by varying the rate of twist of a helicoidal shell. As the main paper's conference format limits its length, it cannot contain all the findings that were made during this thesis. In order to aid any person who wishes to incorporate or continue my work, this thesis contains an extensive appendix in which further observations, experimental results, models and lastly the documentation for the design interface, are described.

Whilst my name may be written under the title, I am far from the only person who had an influence on this work. I would therefore like to start by thanking my supervisor Giuseppe Radaelli, without whose excellent guidance, I would have spent another year or two perfecting the wrong parts, and who graciously printed an astonishing amount of PETG helicoidal shells for me. I would also like to thank Patrick van Holst, with whom I performed the experimental tests, and who was always open to schedule yet another testing day after the many instances of "interesting" results. I would further like to thank my family and friends that lend me their ears and time: Luuk for the invaluable feedback, Chris for hearing me out during all those coffee breaks I will have to miss from now on, Emile and Wim, for listening to my ramblings and supporting me these last few weeks, and finally Rembrandt, Andor, Leon, Iris and Dylan for allowing me to think of things other than the intricacies of transition regions.

I can only hope that you enjoy reading this thesis.

*Tomas Zijm*
*Delft, November 2025*

# Contents

# Designing Tailored Torque-Twist curves using Variable rate of twist Helicoidal shells

Tomas Zijm - 4727363
*Author Supervisor - Dr. Ir. Giuseppe Radaelli*
*Thesis MSC HTE: MNE MSD*
*November, 2025*

***Abstract*—Tailored load-displacement mechanisms are a type of nonlinear mechanisms that can be designed to obtain a specific desired load-displacement curve. In order to achieve tailored torque-twist curves, these mechanisms often need to be complex; requiring multiple parts that sum up to the desired curve. In this work a revolute compliant mechanism, based on a helicoidal shell, is adapted so that it can achieve positive tailored torque-twist curves, using a single part. The goal of this paper is to make a tool that allows this tailorable property to be fully realised using the rate of twist along the spinal axis as the design variable, whilst the radius and thickness are kept constant. This tool has an analytical model as a basis that predicts the numerical result of a Kirchoff-Love shell model. The model is dimensioned by linking numerical results to shape factors of the helicoidal shells as well as observed deflection behaviour. The resulting design method is demonstrated with the creation of a few tailored torque-twist curves: A linearly increasing, as well as a linearly decreasing curve, and two sinusoidal curves, designed to be used as gravity balancers. Subsequently these designs are produced and measured.**

***Index Terms*—Multi-region tailored torque-twist, Compliant revolute Joint, Tailorable Mechanism, Compliant Mechanism, Helicoidal Shells, Neutral Stability**

## II. Introduction

Compliant mechanisms are a class of mechanisms that achieve desired displacements and or loads through carefully designing the geometry of a mechanism, in order to control its compliance. They have many advantageous properties, a selection of which are that they can be monolithic, miniaturised, require no lubrication, experience no friction, and inherently store energy as they deflect[1]. This last property is often undesired as it means that the mechanism requires input energy to achieve the desired stroke. However, it can also be used to one's advantage, for instance in springs, or for a nonlinear spring as a bistable mechanisms.

A nonlinear load-displacement curve, within this paper, refers to a nonlinear load generated by a linear displacement. In addition to bistable mechanisms, Nonlinear load-displacement mechanisms are widely applicable, for example, they are used for force limiters[2], used to balance out gravitational forces [3][4] or the forces needed to deform compliant mechanisms [5][6][7], or they allow for multiple equilibrium positions [8][9] which could be used for mechanical computing[10].
In the literature, tailored load-displacement mechanism can refer to any mechanism that is tuned in a way to achieve the desired curve. Therefore the term Multi-Region Tailorable Torque-Twist (MRTTT) mechanism is introduced. This refers to a mechanism that can be tuned such that it can display multiple behaviours in separate regions. As an example the following curve could be generated: a high load region that is followed by a low load region, which then transitions to a sinusoidal curve, of which the third cycle dips lower than the rest. Whilst there already exist some tailorable load-displacement compliant mechanisms [11] [12], these are mostly summations of multiple nonlinear mechanisms. Instead this paper proposes a single compliant mechanism capable of generating (positive) multi-region tailored torque-twist profiles, using a single mechanism.

The mechanism this work is based on is that of the helicoidal shell studied by Radaelli[13], which works as follows: When the free end is rotated against the twist direction of the helicoid, a constant torque-twist curve is generated. This behaviour stems from two characteristics of the deformation path. The first being that the helicoidal shell has two distinct energetically favourable configurations: The rest configuration and the fully reverse-twisted configuration. The second characteristic is the way the mechanism transitions between these two states. This is achieved by a travelling transition region, which once nucleated travels along the spinal axis. As this transition region travels a mirrored region is formed and expanded. The resultant torque of this expansion is only a result of the deflection happening within the transition region. Due to all the geometric parameters being constant along the spinal axis of these helicoidal shells, the expansion per reverse-twist, and thus the resultant torque, remain constant as well.

The helicoidal shell makes for a promising basis for tailored torque-twist mechanisms as it displays a low axis drift as well as a high Range of Motion. As such, it was used by Abouheidari et al. [14] as a basis to generate a sinusoidal torque-twist curve for use as a gravity balancer. The paper focussed on altering the shell's cross section, adding a flange at the edge. The shape was then computationally optimised to obtain the desired torque-twist curve, iterating the shape input used for the Finite Element Method (FEM).

Iterative shape optimisation methods using FEM, depending on the mesh density and input parameters, takes a long time to yield the desired result. In order to create a faster design method, this paper aims to propose an analytical solution based on the local geometry, which can yield an iteration result almost instantly. FEM analysis can subsequently be used to verify the prediction. If required, the design could then be tuned again manually. In order to set up the analytical prediction equations, FEM results are analysed and coupled to design parameters by means of geometric analysis and curve fitting.

The paper starts in section III-A by introducing the working principle of the helicoidal shell as well introducing a two-dimensional slider model to aid in its interpretation. It also describes the use of an entrance region to control the transition region nucleation. In section III-B the analytical solution is set up, based on observations made from FEM analyses. In section IV the analytical model is compared to the numerical model. This is then followed by the design process for a few tailored helicoids. In section V the designed helicoids are manufactured and experimentally tested, after which these result are compared to the numerical predictions. Then these results, as well as the overall process are discussed insection VI. Finally the findings of this paper are discussed, in section VII, along with their implications on the field as a whole, as well as suggestion for future research.

## III. Method

### A. Working Principles

#### 1) Reverse twisting Helicoidal Shell

The helicoidal shell can be seen as a chain of bistable mechanisms, where every element of the shell has two stable configurations: The base/undeformed geometry and the mirrored/deformed geometry. From this it follows that if the free end is twisted, a mirrored region will start to form, until eventually the entire mechanism consists of the mirrored, energetically favourable, configuration. In Radaelli [13] the geometric parameters of these helicoids were kept constant along the spinal axis, resulting in constant torque-twist mechanisms. If however the geometric parameters are varied along the spinal axis of the mechanism, the result will be a variable torque-twist mechanism. It is this behaviour that will be investigated and modelled in the rest of the paper.

#### 2) Determining the Model Inputs

When observing the results from FEM simulations[15][13] the following observation can be made: if the shells, with a radially constant thickness, expand radially from the centre, whilst the geometric variables radius, thickness and the rate of twist are only varied along the length of the helicoid, then the behaviour scales with the geometric variable values at the outer radial edge of the helicoid. This allows for a conceptual model that simplifies the mechanism by only looking at the geometry of the radial edge.

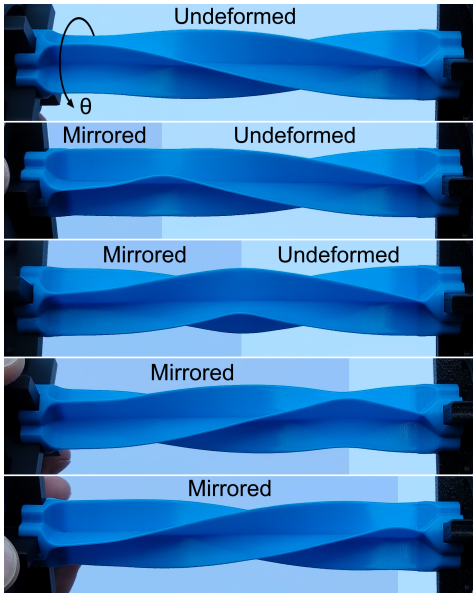


Fig. 1. Deflection behaviour of a helicoidal shell as shown by Radaelli [13]. As one of the endpoints is reverse-twisted a transition region is nucleated, that is the boundary between the undeformed and the mirrored region. Rotating the endpoint further will expand the reversed region, until finally the entire helicoid is reversed as much as it can be.

In order to dimension his model, first imagine the helicoid to have been rolled over a stamp pad, staining the edge, and subsequently rolled out over a sheet of paper. The resulting line where the edge hit the paper is a representation of said edge's geometry. This concept is visualised in Fig. 2. The angle of twist $\phi$ can then be obtained by dividing the axis of travel by the radius of the helicoid. From the resulting graph the main design variable of this paper can be determined: the rate of twist $\alpha$, which for the slice $s$ on the spinal axis along the length is defined as follows:

$$\alpha_s = \phi'_s = \frac{\delta\phi_s}{\delta L_s} = \frac{\Delta\phi_s}{\Delta L_s} \tag{1}$$

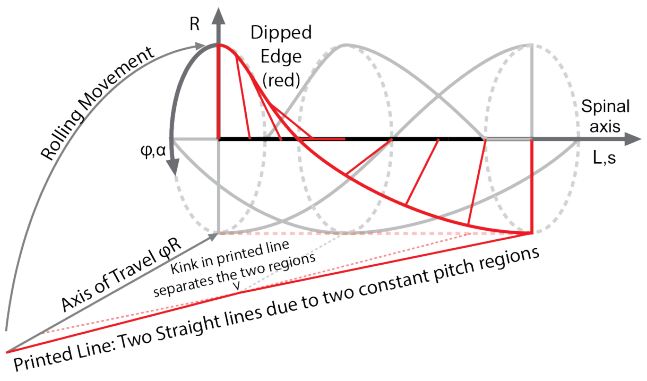


Fig. 2. A helicoid is shown on its side. The red edge has been stained and has left a red line on the surface as it was rolled over it. This line consists of two straight lines with different angles, as the helicoid is made out of two different constant rate of twist regions. The printed lines are extended with a thin red dotted line in order to show the difference between the two regions. In addition the spatial shape of a shell of the helicoid is made clearer by adding red ribs extending from the spine.

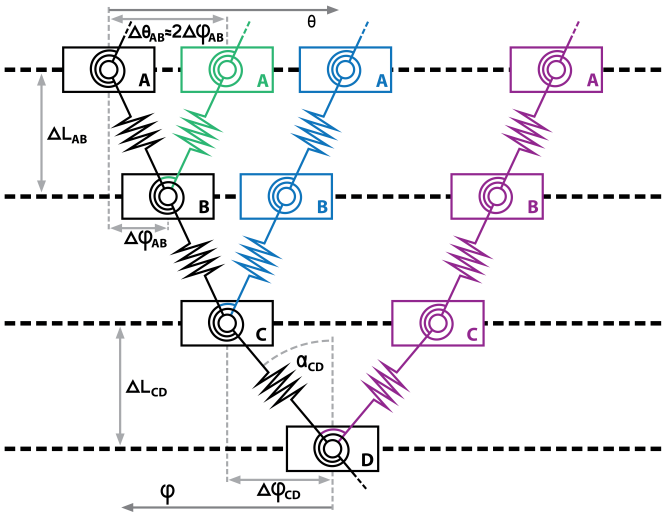


Fig. 3. A visualisation of the Links and Sliders model for a variable rate of twist helicoid. The The black geometry is the starting geometry. It consists out of horizontal parallel sliders that are connected by linear springs, which are interconnected by revolute springs. In this starting configuration the transition region has reached the top(left) slider from above. As the top slider is moved to the right the transition region travels down the links, shown in the subsequent colours: teal, blue and lastly purple. The figure also demonstrates the definition of the rate of twist $\alpha$ between slider C and D.

### 3) Links and Sliders Model Description

The rolled out edge line, after having been divided by the radius, can be conceptually subdivided into an arbitrary amount of parallel sliders connected by links as seen in Fig. 3. Every link consists of a linear spring, and is connected to the chained links by revolute springs. The linear spring allows for the bistable behaviour of the helicoid, where if the top slider is moved to the right these springs are compressed until, in an imperfect system, the weakest link snaps into the mirrored stable position. The connecting revolute springs store this snapping energy, and therefore allow for the previous snapping step to affect the next, forming the transition regions. In the constant rate of twist helicoids investigated by Radaelli[13] the energy stored in the transition region remains constant, throughout the constant torque region, and can therefore be ignored. However, when the rate of twist is varied along the spinal axis, the energy stored in the transition region will vary as well. This makes this component crucial to understanding the situation in variable rate of twist helicoids.

In order to explain the working of a travelling transition region along a varying rate of twist helicoid, the process is explained in three steps, as shown in Fig. 4. Here the situation in step 1 is the initial rest configuration for slider C. Step 2 shows the torsion spring in slider C being torted due to slicer B being snapped to the right. Since following slider (D) has a longer path to travel, than the previous slider (B), before it reaches the final rest position, it requires more energy to reach it. This movement additionally increases

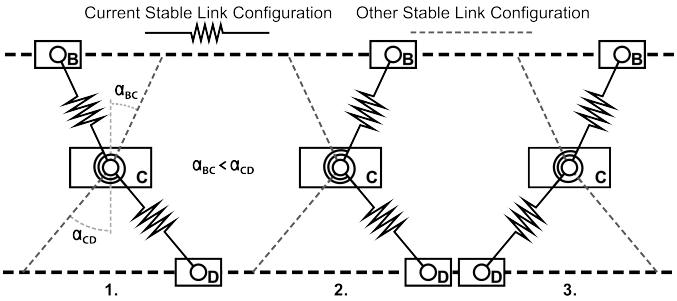


Fig. 4. The three states of the links around slider C from Fig. 3. Going from 1 to 3 shows the transition region moving from top to bottom, experiencing an increase in the local twist angle. Going from 3 to 1 shows the transition region moving from bottom to top, experiencing a decrease in the local twist angle.

the displacement of the revolute spring. This results in a behaviour where deflecting a next element that has a higher rate of twist requires additional energy than when only the difference between the linear springs is considered. The opposite behaviour can be expected if the order of the images is reversed, so that the following slider has a shorter path than the previous. Here the energy needed for this deflection would be lower than if only the difference between the linear springs had been taken into account. This is exactly the behaviour that we will observe later in the paper when the rate of twist is varied along the curve.

### 4) Controlling the transition region

The main obstacle to the range of tailored torque-twist profiles a helicoidal shell can make, is that the mirrored region will nucleate and expand where it takes the least amount of energy to do so. This means that it will only expand into the higher deflection energy regions once that finally becomes the easiest path. This is shown using the rate of twist in Fig. 5. This complicates the design process if a lower torque twist region is desired later in the stroke than a higher region.

Controlling the transition nucleation is the main reason why this paper has chosen to use the rate of twist as the main design variable: Contrary to the thickness or radius, the rate of twist can have a value of zero. This allows the designer to dictate the location where the transition region nucleates, as the zero rate of twist point will be the most energy advantageous spot. The best strategy is to taper the rate of twist to zero towards either the fixed or free end, as this causes only a single transition region to nucleate. Once nucleated, the transition region is forced to travel along any designed shape, as long as its continued travel requires less torque than it would for a second transition region to nucleate further down the spine. This means that, within limits, a lower torque region after a higher torque region becomes possible as is shown in Fig. 6.

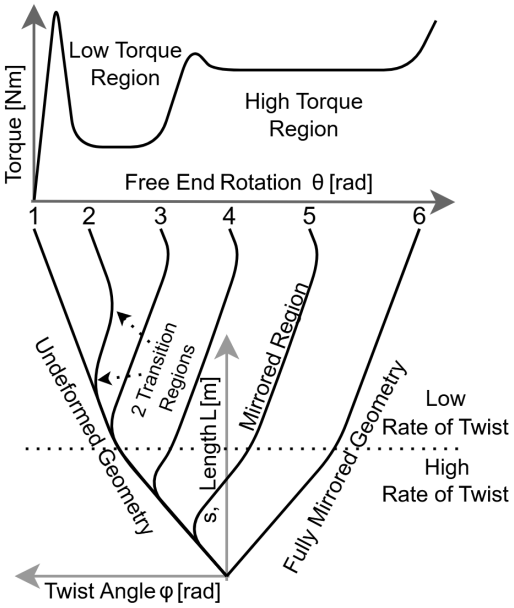


Fig. 5. Varying rate of twist helicoidal shell. The top shows the torque-twist curve generated by the geometry shown below. As the end effector is rotated (moved to the right) it travels along the points 1 to 6. Both parts of the figure share the same free end motion axis. 1. The initial undeformed geometry. 2. Two transition regions are created in the low rate of twist region. 3. The mirrored region expands throughout the entire low rate of twist region before reaching the high rate of twist region. 4. The mirrored region expands into the high rate of twist region generating a higher torque. 5. The mirrored region continues to expand into the high rate of twist region. 6. The Geometry is fully mirrored.

TABLE I
MATERIAL PROPERTIES OF PETG PRINTED IN THE Z DIRECTION AS GIVEN BY ULTIMAKER [16] AND MERCADO-COLMENERO ET AL. [17].

| Property | Value | Unit |
|---|---|---|
| Young's Modulus | 1.7 | GPa |
| Poisson's Ratio | 0.38 | - |

*5) Finite Element Model*

The Finite Element Model that serves as the basis for the analytical solution is a MATLAB implementation based on the work of Nagy et al.[15], and further adapted by Radaelli [13]. This model is based on a Kirchhoff-Love shell with a linear elastic constitutive law. It evaluates a single shell with constraints and loads applied as shown in Fig 7. The material properties are taken to be that of PETG printed in the z-direction and are shown in Table I. As the manufacturer (RealFilament) does not provide a comprehensive data sheet these values are taken from comparable materials.

## B. Setting up the Equation

*1) Defining the Equation components*

As mentioned prior, the resulting torque can be seen as the combination of the rate of twist and the difference between adjacent twist angles i.e. its derivative. This concept is visualised in Fig. 8 (a), where the rate of twist, its derivative and the sum of the two are plotted to generate the torque shape along the length of the helicoid. To convert this to the

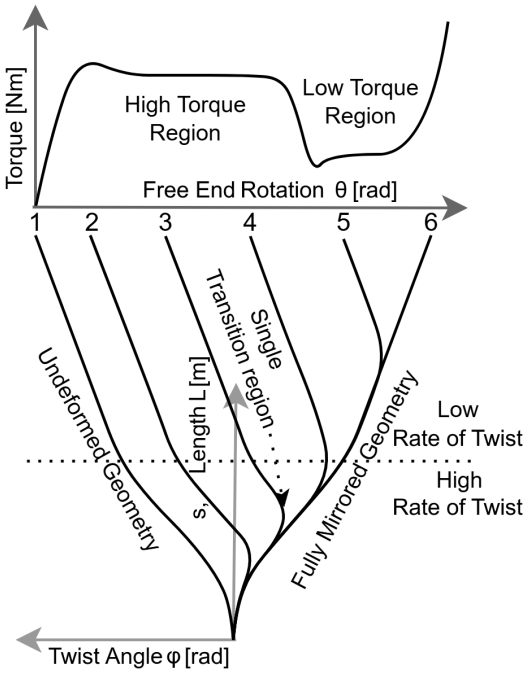


Fig. 6. Varying rate of twist with the rate of twist tapering to zero towards the endpoint. The top shows the torque twist curve generated by the geometry shown below. As the end effector is rotated (moved to the right) it travels along the points 1 to 6. Both parts of the figure share the same free end motion axis. 1. The initial undeformed geometry. 2. The transition region starts from the zero rate of twist point at the bottom endpoint, creating a gradual increase in torque. 3. The transition region has entered the high constant torque region. 4. The transition region reaches the transition between the high and low rate of twist regions. 5. The transition region is expanding within the low constant torque region. 6. The geometry is fully mirrored.

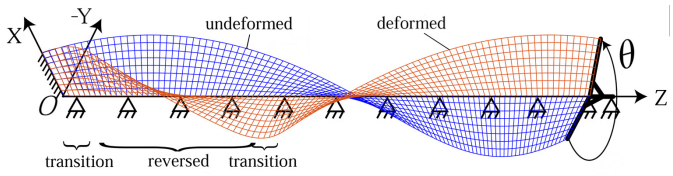


Fig. 7. The Finite Element Model of the helicoidal shell, setup by Radaelli [13], is shown, it consists of a single shell, rotationally constrained around the spinal axis. A clamping constrained is applied to the fixed edge, whilst a rotating clamping constraint is applied to the free end. The blue curve signifies the undeformed state, whilst the red signifies the deformed state when the free end is rotated by $\theta$.

torque-twist approximation the rate of twist and its derivative are multiplied by scaling factors $f_\alpha$ and $f_{\alpha'}$. This equation is defined by the position of the slice or slider coordinate $s$ along the spine axis. Due to the difference between the rest and mirrored configuration being $2\phi_s$, the equation also needs to be multiplied by two. A further constant $C_{Sh}$ is required, this is the shell constant including the material properties and as the shell thickness. The amount of shells per mechanism is defined by $N$. The resulting Torque equation can be defined as follows:

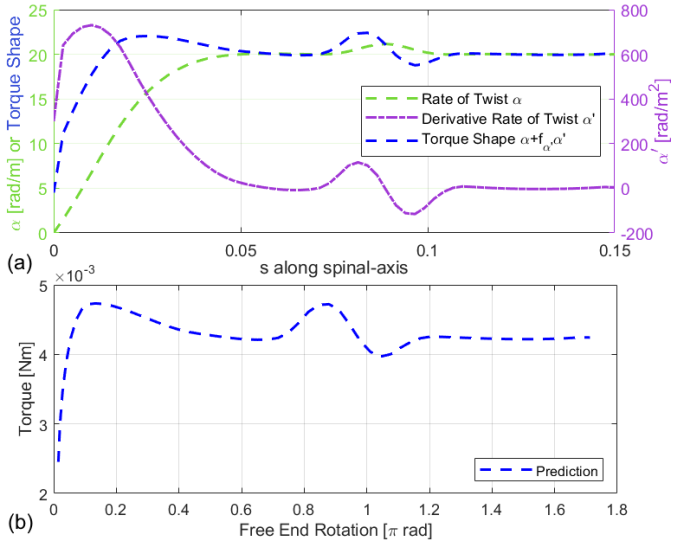


Fig. 8. Prediction of the torque-twist curve visualised. The top figure (a) shows the design variable, $\alpha$, the rate of twist axis, along the spinal axis of the helicoid, as well as its derivative $\alpha'$ and the summation (including scaling coefficient $f_{\alpha'}$). The bottom figure shows the Torque-Twist prediction compared to the FEM result. These results were obtained with a radius of 12.5 mm and a shell thickness of 0.4 mm. In the entrance behaviour a difference can be observed, this stems from a hard to model combination of the transition region size and the pure torsional compliance term.

$$T_s = NC_{Sh}2(f_\alpha \alpha_s + f_{\alpha'}\alpha'_s) \tag{2}$$

In order to determine the value for $\theta$ reached when the transition region is at spinal axis coordinate $s$ a second equation needs to be set up. The main contribution to the Range of Motion (ROM) of the free end is visualised in Fig. 6, namely the twist angle $\alpha$ at $s$. This value needs to be doubled as the mirrored equilibrium position is reached by travelling that distance twice. The travel is however also affected a Saint-Venant torsion stiffness component, that adds additional twist for a value of torque. This combination results in the following equation for the travel of the free end $\theta$:

$$\theta_s = 2\phi_s + T_s/K_{\text{SV}} \tag{3}$$

Combining these two equations results in the torque-twist curve as shown in Fig. 8(b). These equations must be understood to be limited in their applicability within a certain range of geometric variables. Nor does it always accurately model the behaviour at the beginning and endpoint of the curve. This is due to the model sampling a single slice, where in truth the entire transition region has an effect on the torque. A region whose size is determined by said geometric variables. This transition region also affects the SaintVenant stiffness term as it is expected to have a stiffening effect on its area of effect. Within this work that effect is simply corrected by a manually applied correction factor.

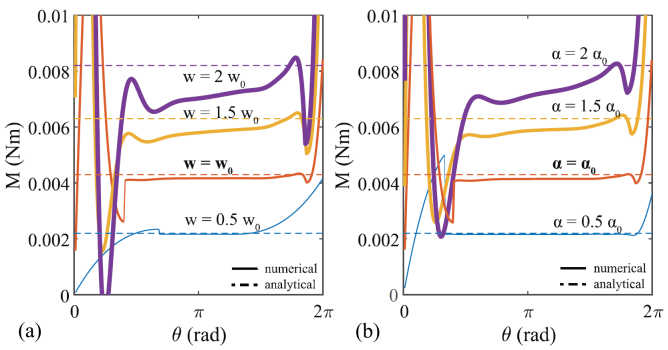


Fig. 9. Radius and rate of twist scaling results as shown in Radaelli [13]. It can be observed that the torque for both Radius and rate of twist scale in the same nonlinearly increasing manner.

*2) Shell Constant $C_{Sh}$*

Radaelli [13] states, due to the condition of inextensibility and the constraints that hold the shell in the centre, that Calladine's definition of the strain energy of bending per unit area of a shell [18] can be simplified to only take the energy contribution from the change of twist into account. Thus giving the following equation:

$$U_B = 1/2D[2(1-\nu)\kappa_{xy}^2] \tag{4}$$

Where $\kappa_{xy}$ is the change in twist curvature, defined as $2(f_\alpha \alpha_s + f_{\alpha'}\alpha'_s)$, and $D$ is the flexural modulus given by:

$$D = \frac{Et^3}{12(1-\nu^2)} \tag{5}$$

It consists of E: the Young's modulus, and $\nu_{12}$: the Poisson's ratio. From (4) we can isolate the Torque resulting from twist $T_{xy}$, using $U = \int T_{xy}\delta\kappa_{xy}$, which yields $T_{xy} = D(1-\nu)\kappa_{xy}$. This can be simplified to $1/6Gt^3\kappa_{xy}$ where G is the shearmodulus given by $G = \frac{E}{2(1+\nu_{12})}$. Where $E$ is the Young's Modulus and $\nu$ is the Poisson's ratio. This yields the following solution for the shell constant:

$$C_{\text{Sh}} = 1/6Gt^3 = 1/6\frac{E}{2(1+\nu)}t^3 \tag{6}$$

*3) Constant Rate of Twist/Bistable Component $f_\alpha \alpha \rightarrow f_{BS}$*

Radaelli[13] proposes a torque prediction model that suggests a linear increase with rate of twist and radius. This model however accumulates an error if the range is increased, as shown in shown in Fig. 9. If the FEM results in the model are observed further an observation can be made: Interestingly, varying the radius or the rate of twist by equal amounts results in the same torque. Further FEM tests show that if for any values of the rate of twist and the radius, the multiplication results in the same value, the resulting torque will as well. These two behaviours suggest that they are components of an angle. This angle is determined to be the tangent of the outer edge of the shell $\beta$, as visualised in Fig. 10. This term comes to replace the term $\alpha_s$ in equation 2 In a discrete manner this angle can be calculated as follows:

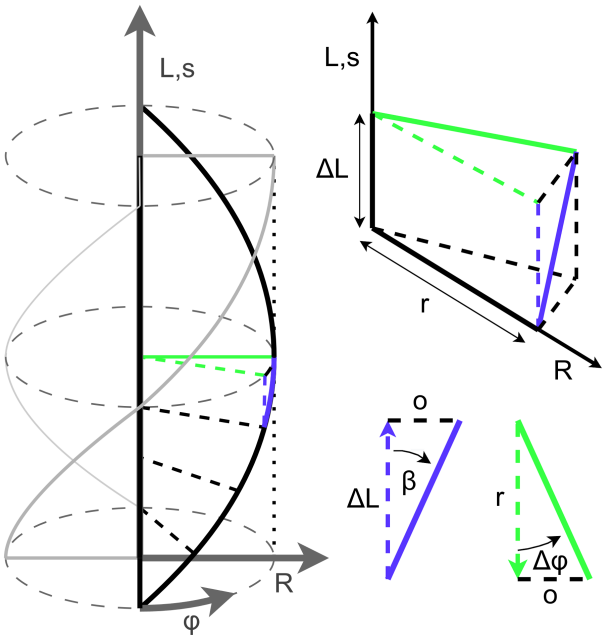


Fig. 10. Left: Helicoid showing the dimensions and framing part of the curve shown in the top right. This part in turn frames the coloured planes that determine the edge tangent angle $\beta$. From this figure it can be observed that the angle $\beta$ starts at 0 at the spine and increases as the radial coordinate is increased.

$$\beta = atan\left(\frac{o}{\Delta L}\right) = atan\left(\frac{\Delta\phi}{\Delta L}r\right) = atan(\alpha r) \tag{7}$$

Where o is the circumferential arc-length given by:

$$o = \Delta\phi\, r \tag{8}$$

and $\alpha$ is again the rate of twist given by:

$$\alpha = \frac{\Delta\phi}{\Delta L} \tag{9}$$

In order to verify that this prediction of $\beta$ scaling is correct, a wide range of constant rate of twist helicoids, with shell thickness of 0.4 mm, is simulated. These result in 9 values for $\beta$ achieved by 8 $\alpha$ and 9 Radius steps. The base values were set at $\alpha$ = 10 rad/m, and R = 10 mm. Each scaling step, the value was multiplied by a factor of 1.2. In order to get 9 $\beta$ values, for each increase of the radius by 1.2, the base value for $\alpha$ was divided by 1.2. In order to scale $\alpha$ the total twist was scaled rather than the length. This was done to minimise the range on which the transition region was influenced by the edge. The lower bound for $\beta$ was set such that a small constant torque region was still able to form. The resulting steps are thus as follows:

$$R(i) = 1.2^n R_{start}, \quad with \quad n = -2:7 \tag{10}$$

$$\alpha(n,i) = 1.2^{i-n+2}\alpha_{start}, \tag{11}$$

$$with \quad n = -2:7 \quad i = -2:8$$

The Torque prediction made using $\beta$ comes close to the results given by the FEM calculations. This resulted, within the sampled range, in a maximum difference of 3% at higher values for $\beta$. The goal of the thesis is however to create a program that could reliably predict the FEM results, and as such a correction coefficient was determined.

A potential origin of the difference is supposed to be the in-slice deflection caused by the transition region, where the edge at the centre of the region is forced to deflect inwards, thus changing the direction and moment arm of the shear forces that cause the mirroring. The in-slice deflection angle is hereby defined as $\gamma$, and is the angle of a point along the radius compared to the angle of the spine. This deflection also results in a decreased effective moment arm, which is denoted as $R_{eff}$. Thus the corrected bistable component $f_{\mathrm{BS}}$ becomes:

$$f_{\mathrm{BS}\,s}(\beta_s, \gamma_s) = \beta\, cos(\gamma_s)\frac{R_{\mathrm{eff}\,s}}{R} \tag{12}$$

However, the angle $\gamma$ remains only determinable, after a FEM simulation, rather than predictable. The determined value is furthermore made unreliable by the behaviour of the spine, which, at higher ratios of radius and rate of twist to shell thickness, torts. As it is torted following orientation of the edge, the measured value for $\gamma$ is decreased.

In order to avoid using $\gamma$, a different correction factor is determined. This coefficient uses the fact that for any constant rate of twist geometry that has the same value for $\beta$ the resulting torque will be almost the same. From this it follows that the correction coefficient only requires $\beta$ as an input variable. Using this principle, the following corrected bistable component $f_{\mathrm{BS}\,s}$ is determined.

$$f_{\mathrm{BS}\,s}(\beta) = \beta\, cos(\beta)^{\cdot 3} \tag{13}$$

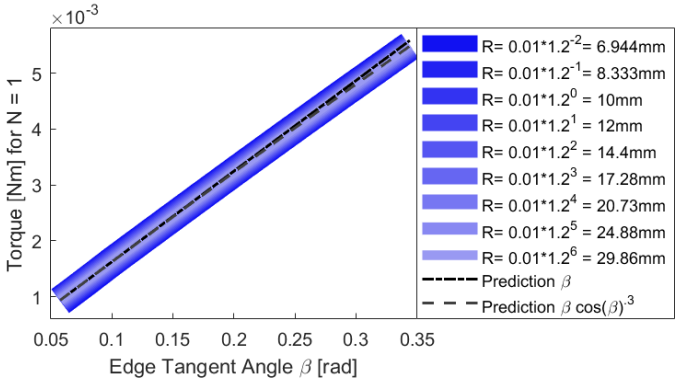


Fig. 11. Constant torque region values obtained from FEM calculations plotted for $\beta$ scaling. 9 lines consisting of increasing rate of twist (and thus $\beta$) are plotted. Each line is a certain radius increment. The plotted lines show a clear trend line as all lines largely overlap. The dashed lines are the predictions $\beta$ and $\beta cos(\beta)^{\cdot 3}$. A clear difference can be observed in the quality of the prediction, where the corrected prediction follows the curves almost exactly.

*4) Variable Rate of Twist / Transition Region Component* $f_{\alpha'}\alpha' \rightarrow f_{TR}$

The derivative of the rate of twist can largely be predicted using a point model, though it cannot be predicted exactly. This stems from the root of the derivative, as a part of its characteristics stems from the size of the transition region depending on the rate of twist itself. A secondary complicating effect is the torsional compliance of the entire helicoid also having an effect on the slope of the curve. Although a perfect prediction is not possible, a useful approximation is. This approximation was derived from observation. The derivative part of the prediction formula relies on smooth/continuous $\alpha$ curves as any geometrical discontinuities would have affected the transition region long before it reaches the sampling point of this model. A solution for this is to use splines as the input for $\alpha$.

$$f_{\alpha'}\alpha' = \alpha' R^2 cos(\beta)^{\cdot 3} \tag{14}$$

This alone will yield differences with the FEM of up to 10%, therefore a second component is determined. This component stems from the derivative of the bistable component $f_{\text{BS}}$ with regards to the rate of twist.

$$\frac{\delta f_{\text{BS}\,s}(\beta)}{\delta\alpha} = \beta' cos(\beta)^{\cdot 3} - 0.3\alpha R\beta\beta' cos(\beta)^{\cdot 3} \tag{15}$$

Where $\beta'$ due to R being constant is given by:

$$\beta'_s = \frac{\alpha'_s R}{1 + (\alpha_s R)^2} \tag{16}$$

The second component is subsequently made unit-less by multiplying it by $R$. Equation 14 and 15 can then be combined as follows, forming the transition region component $f_{\text{TR}\,s}$:

$$f_{\text{TR}\,s}(\alpha') = f_{\alpha'}\alpha' + \frac{1}{8} R \frac{\delta f_{\text{BS}\,s}}{\delta\alpha} \tag{17}$$

Filling in and simplifying yields the final equation:

$$f_{\text{TR}\,s}(\alpha'_s) = 2cos(\beta_s)^{\cdot 3} R^2 \alpha'_s + \frac{1}{8} R\beta'_s(1 - \alpha_s R\beta_s) \tag{18}$$

*5) Saint-Venant torsion Stiffness*

As the determining of an analytical solution for the axial stiffness of a helicoidal shell falls outside the scope of this work, a simpler model is made. The model uses saved numerical results of a wide range of constant rate of twist helicoids as a lookup table. These helicoids are varied in their rate of twist as well as their radius. To obtain their polar moment of inertia J they are twisted in the positive twist direction. The result of which is shown in Fig. 31.

In order to obtain the Saint-Venant stiffness term, the designed helicoid is divided into slices along its spinal axis. For each slice the polar moment of inertia is determined by finding that of an equivalent constant rate of twist helicoid from the lookup table. Then all these slices are combined to create the

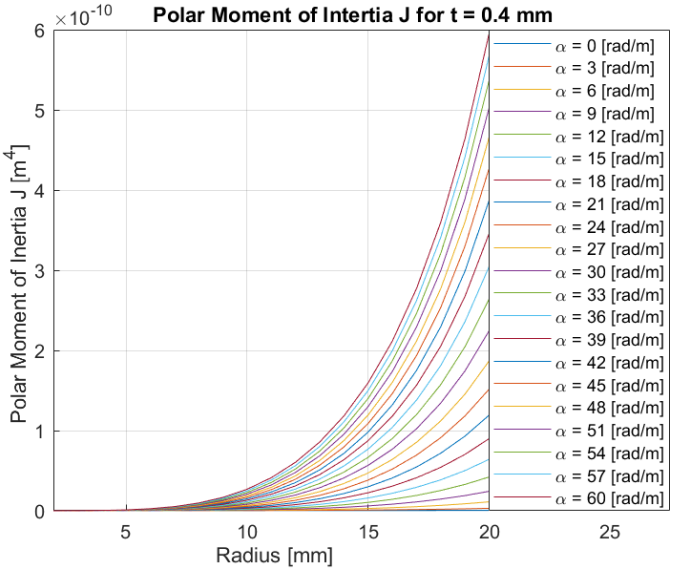


Fig. 12. Polar moment of inertia J determined with a shell thickness of 0.4 mm.

Saint-Venant stiffness of the entire helicoidal shell, using the following equation.

$$K_{\text{SV}} = \frac{G}{\sum_{s=0}^{s=L} \frac{l_s}{J_s}} \tag{19}$$

A shortcoming of this stiffness model is that is does not take the transition region into account. The transition region is expected to have a stiffening effect on its area of influence. The stiffness model therefore needs to be manually corrected by a factor $\kappa_{\text{SV}}$, once the first FEM verification has been performed, as it is more compliant than it should be. For a further explanation of the model the reader is invited to inspect Appendix D, where the results of Fig. 31 are also tabulated in Table IV and Table V.

*6) Combined Equation*

Combining the defined components results in the prediction for the torque at a specific slice along the spinal axis, for a constant thickness and radius but variable rate of twist helicoidal shell.

$$T_s = NC_{\text{Sh}}(f_{BS}(\beta_s) + f_{\text{TR}}(\alpha'_s)) \tag{20}$$

Inserting equations (13) and (18) and simplifying yields.

$$T_s = NC_{\text{Sh}} 2cos(\beta_s)^{\cdot 3}(\beta_s + R^2\alpha'_s + \frac{1}{8} R\beta'_s(1 - 0.3\alpha_s R\beta_s)) \tag{21}$$

Where the twist that the free end has when the transition region is at slice $s$ can be determined by the following equation mentioned earlier.

$$\theta_s = 2\phi_s + T_s / K_{\text{SV}} \tag{22}$$

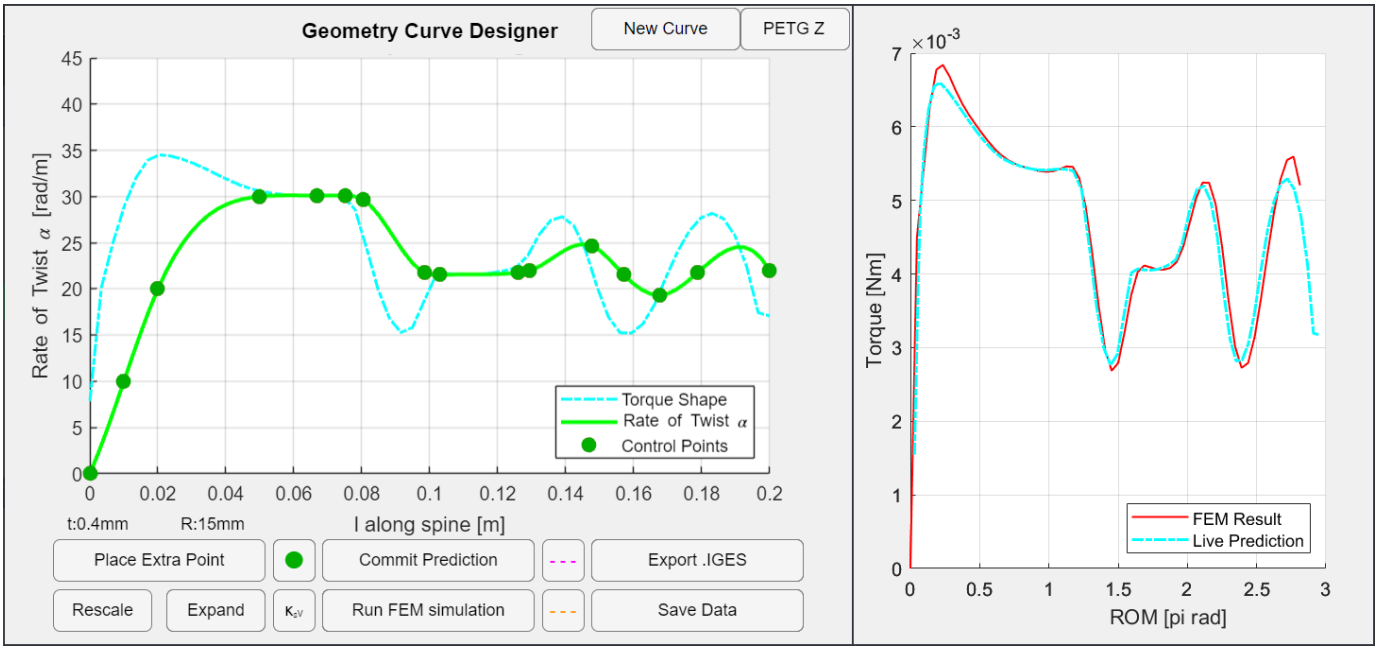


Fig. 13. Design Software Interface used to design torque-twist curves. The example here is that of an MRTTT curve. On the left is the design interface, where the red control points can be dragged in order to affect the rate of twist spline. A live Torque shape will be shown in the same window, as well as in the window on the right. Here one can also plot guide curves to follow. Once the predicted curve is close to the desired one, a FEM simulation can be used to verify the Torque-Twist curve, after which manual iterations can be performed to get the FEM result to where it is desired. The design interface will be further discussed in Appendix. H.

## IV. Results

### A. Design Software

In order to fully realise the potential of these equations, a design interface was made in MATLAB. In this interface the user can indirectly design a torque curve by manually controlling the rate of twist along the spine length. The program can then plot this prediction after which it can be verified using a FEM calculation. Once the resulting torque profile has been achieved it can be exported and printed. The interface of this program is shown in Fig. 43, where it is used to design a MRTTT curve. For a full documentation of the design interface, the reader is invited to read Appendix H.

### B. Model Verification

Having set up the analytical equations for a shell thickness of 0.4 mm, the effectiveness of the design method can be displayed by showing the effect of the components on the MRTTT curve designed in IV-A, and comparing them to the FEM result. This process is shown in Fig. 14.

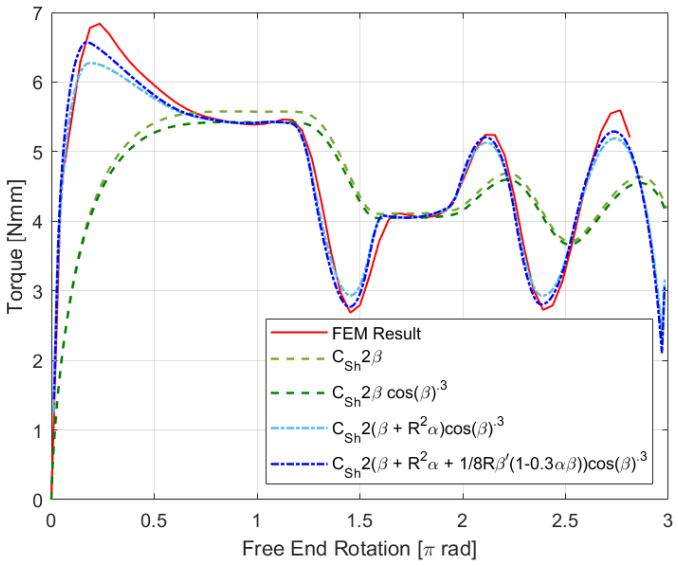


Fig. 14. The verification of the different torque equation components, where the effect of each component can be observed to improve the prediction.

### C. Torque-Twist curve examples

To further illustrate the capability of the design method, the design interface shown in Section IV-A is used to create a set of torque-twist curves. The first sub-set are constant torque-twist profiles, whilst the second sub-set are tailored torque-twist profiles. These designs were chosen for their possibility of being manufactured and experimentally measured, a process which is shown in Section V.

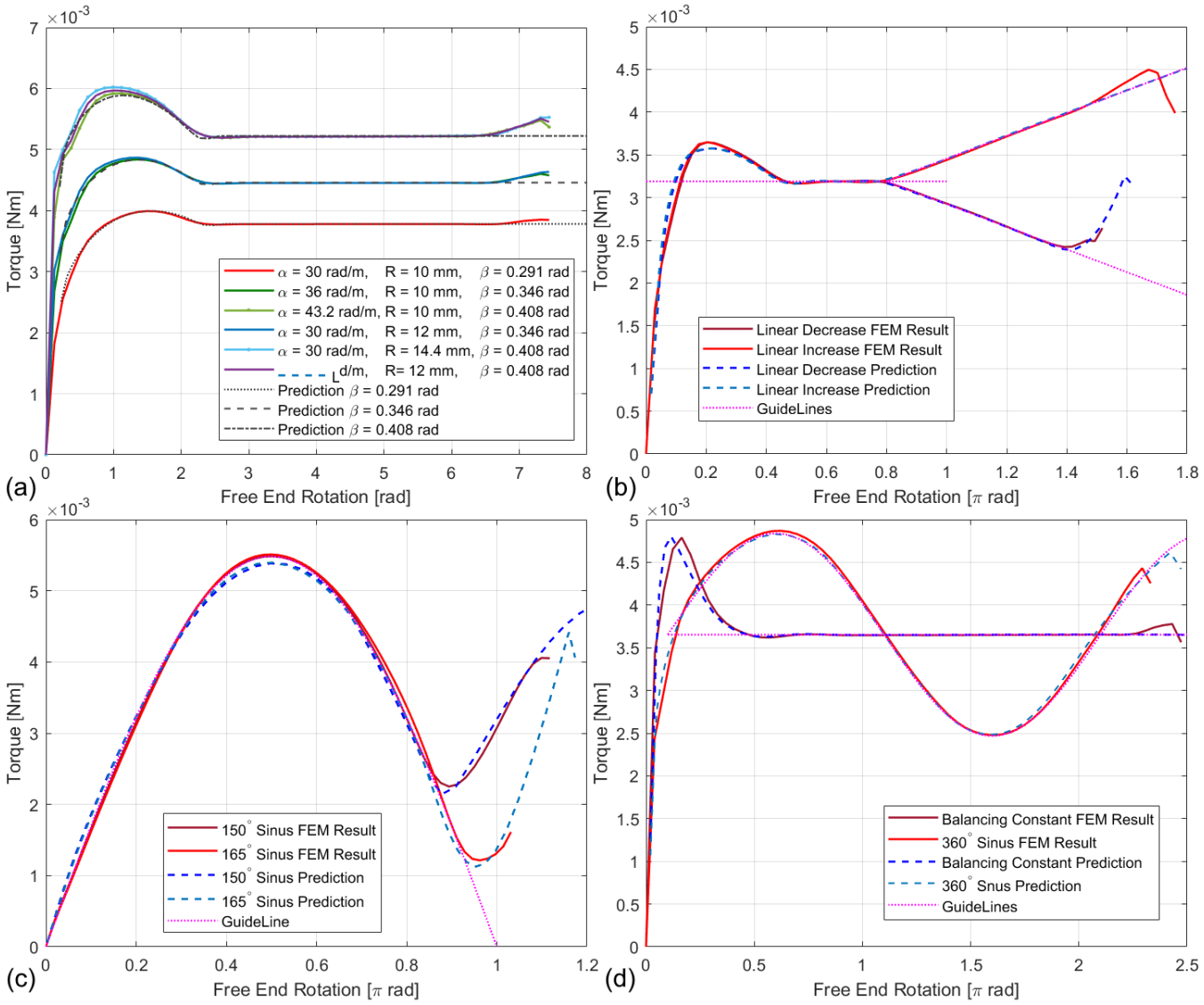


Fig. 15. Torque-twist curves of the geometries to be tested. (a) Contains the scaled constant torque curves to validate the $\beta$ scaling hypothesis. (b) Contains curves that show that both a linearly increasing as well as a linearly decreasing torque curves are possible. (c). Contains two gravity balancer curves that follow the first 150° and 165° of a sine wave. (d) Shows the curves for a 360° gravity balancer, where an elevated sinus is balanced out by a prestressed constant torque helicoid.

*1) Constant Torque-Twist Profiles*

In order to verify the torque scaling with $\beta$ a few scaling steps were designed: First an unscaled helicoid as a basal reference was made with $\alpha$ = 30 rad/m and R = 10 mm. Then 4 helicoids that either scaled the rate of twist $\alpha$ (by decreasing $\Delta L$) or the Radius. Next, to show $\beta$ being the determining factor a helicoid where both variables were only scaled once was also made, such that the resulting torque should equal the helicoids that have one variable scaled twice. The scaling factor used is 1.2, which is the same as is used to verify the constant rate of twist component $f_{BS}$. This was kept relatively low in order to limit the highest torque values, in order to keep the helicoids from breaking due to internal stresses in the subsequent case studies in section V.

*2) Tailored Torque-Twist Curves*

The design method was further used to design a range of curves shown in Fig. 15(b-d): First a linearly increasing and a linearly decreasing curve, are designed, starting from a constant torque region (b). These demonstrate the reasonably narrow range of effect of the transition region, validating the point-model used. The narrow range of effect also allows the helicoid to quickly switch between behaviours. Then two attempts are made to create a 180° gravity balancer (c), the first being a conservative version that follows the curve up to 150°, second version that follows the curve up to 165°. The second version was designed by incrementally increasing the range up until a second transition region was nucleated. The conservative version was made to be manufactured in

the section V, as manufacturing inconsistencies could cause a second region to nucleate earlier than the FEM predicts. Lastly a 360° gravity balancer is designed (d). In order to achieve this two helicoids are required: A first that generates an elevated sinusoidal curve connected to a second that generates a constant torque-twist curve. When the second helicoid is fully reverse twisted it adds a negative torque equal to the average of the sinusoidal curve. The summation of the two helicoids results in, slightly more than, a complete cycle of a sinusoidal wave around the zero torque axis.

## V. Case Studies

Whilst the goal of the paper is to showcase a faster design method for tailored torque-twist curves, a further step into experimental verification is also performed.

### A. Material and production choice

The material and manufacturing method chosen are that of PETG Filament Deposition Modeling (FDM). Of the filaments available for FDM printing, PETG prints well and has relatively good interlayer adhesion[19]. This choice was made after initial investigations with other materials yielded poor results. These findings are expanded upon in Appendix E. The interlayer adhesion is especially important as the helicoids were printed with the spine oriented vertically. This orientation was chosen in order avoid any supports, as these could leave inconsistencies even after having been removed. Printing in this orientation also ensures that there is a uniform load across a slice. The downside is that the load goes across the layer lines, leaving the helicoids fragile. A thickness of .4 mm is chosen as a sweet spot, printed by 2 adjacent lines with a .2 mm nozzle. For the amount of shells N per sample, 4 was chosen.

### B. Experimental Measurements

#### 1) Constant Torque-Twist curves

For the constant torque helicoids the shown displacements are reduced from the total measured strokes, as some helicoids had a shell fail close to $\theta_{ROM}$. In these situations the working principles of the helicoids keep the data from becoming unusable, as for most of the forward and backward stroke, the transition region remains unaffected by the breakage. Therefore the only measurable difference becomes the Saint-Venant stiffness term, which shifts the entire curve as the helicoid deflects more. Each constant helicoid was produced multiple times but of most types only two remained intact at the moment of the experiment. Of the second radius and the second rate of twist scaling step, however, three samples are measured. The results shown in Fig. 17 are the average of the results from the helicoids with the same designed geometry. Every helicoid is tested thrice consecutively. It is observed that the inclusion of an entrance region largely removes the initial peak present for the constant rate of twist helicoids studied by Radaelli [13]. Although it does not follow the predicted shape, instead being compressed to a narrow peak. Comparing the scaled helicoids shows a clear constant torque increase for every scaling step, resulting in largely overlapping results for the same value of the edge tangent angle $\beta$. However, the actual increases per step fall short of the roughly 1.2 times increase expected.

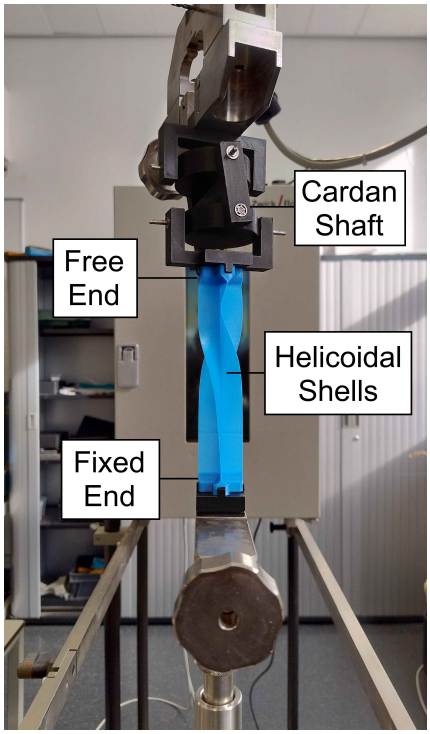


Fig. 16. Helicoid in the test setup mid stroke. A cardan shaft connects the top to the torque bench.

#### 2) Tailored Torque-Twist curves

The linear increase and decrease, shown in Fig. 18(a), clearly demonstrate a variability in the printed shell thickness. Even though the results are the averages of a pairing of the two geometries printed twice, the ondulations of the initial curves overlap nearly exactly. For the 180° and the 360° sinusoidal curves only one sample remained intact during the experiments. The result of the balancing constant in Fig. 18(c) is an average of two separate curves.

## VI. Discussion

### A. Predictive Model

The analytical solution gives a reasonable prediction of the FEM result. For constant torque regions the highest error remains under 0.5%. However the differential component remains relatively inaccurate, with a slightly bigger error of 4%. This could stem from the fact that the interaction between the transition region and the spine remains unmodelled. Nor does it model the interaction of the transition region with the rigid interface between the shells and the free or base end.

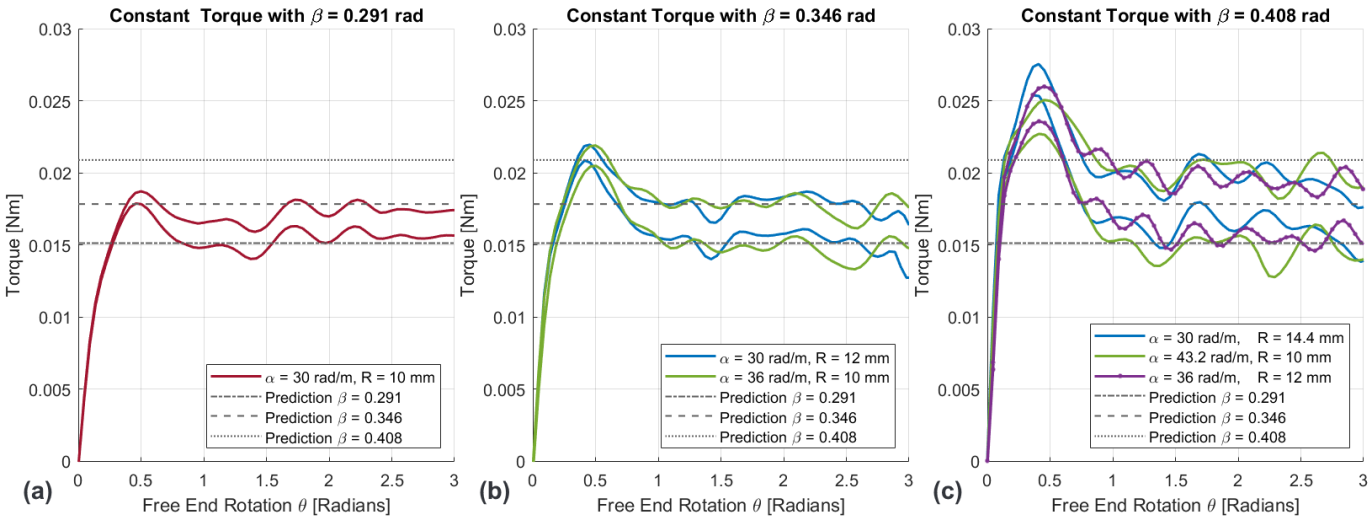


Fig. 17. Experimental torque-twist results of the $\beta$ scaling tests, compared to the predicted constant region values. (a) shows the base geometry (b) The first scaled step. (c) show the second scaling step for each separate variable as well as the first scaling step if both variables are scaled simultaneously. All torque results are higher than the expected value.

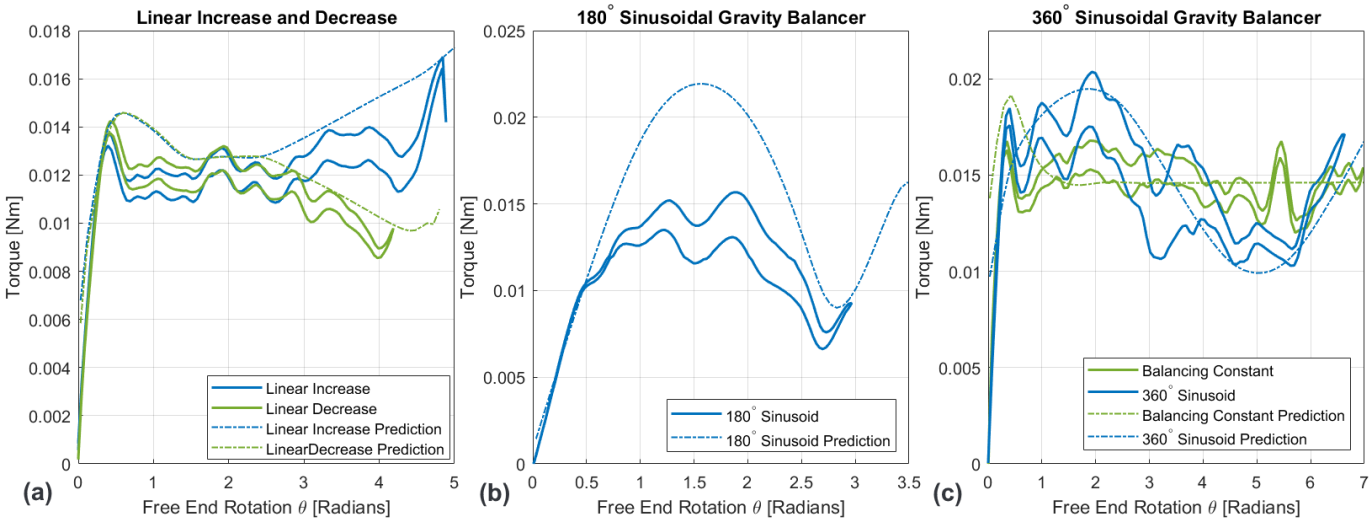


Fig. 18. Experimental Torsion results compared to the FEM results. With (a) being the linearly decreasing and increasing curves, (b) being the 180° gravity balancer, and (c) being the 360° gravity balancer with the balancing constant torque.

As the analytical model is based on the behaviour of a single transition region travelling along the spinal axis, it therefore cannot be used for helicoids with multiple transition regions, nor can it predict when a second transition zone is nucleated. This means that a rule of thumb needs to be adhered to, not to make a torque region lower than a third of the highest preceding value. Although local valleys can sometimes reach lower ratios. Furthermore, the model cannot accurately predict the return stroke, where it is possible that a second transition region is nucleated from the zero rate of twist region.

The Saint-Venant stiffness model using a lookup table is sufficient when a multiple constant torque-twist region mechanism is designed, or when tailored curves that keep the rate of twist variation relatively limited. An example of which is the 360° gravity balancer sinusoidal curve. The model however, does require a correction for high rate of twist variability curves, such as for the design of the 180° sinusoidal gravity balancer. These inaccuracies stem primarily from a stiffening effect in the transition region, that is not included in the prediction.

### B. Experimental Results

The test results show large differences between the analytically predicted/FEM results and those obtained by experimental measurement of the FDM printed helicoids. This could be due to a variety of reasons. The first being that the produced shell thickness is not constant along the length. As such other shell thickness inconsistencies between prints could also be possible. Due to the helicoidal shells being printed vertically using FDM, with no surface smoothening step, the effective thickness could be thinner than the designed thickness, or even than the measured thickness. The effect of the printed material properties is expanded upon with a series of 3-point bending tests in Appendix F.

Although the constant $\alpha$ scaling steps show an increase in torque for every step, the hysteresis is within the same magnitude as the increase. This makes the pattern less clear. Instead, a larger scaling step could have been used, tuning the starting variables to ensure that the second scaling step doesn't break.

The measured 180° sinusoidal curve, shown in Fig. 18(b), differs greatly from the designed curve. This difference could be due to the nonlinear force to strain response for higher values of strain. This nonlinearly elastic behaviour is expanded upon in Appendix E.

## VII. Conclusions and Recommendations

In this paper the reverse twisting helicoidal shell studied by Radaelli [13] is expanded upon. Where Radaelli used the properties of the helicoid to generate constant torque-twist curves, here its capability to generate tailored torque-twist curves is investigated. Using rate of twist variation proves to be a powerful method, as the resultant torque of the reverse twisted helicoid is only generated by the geometry inside a travelling transition region. This is enabled by controlling the nucleation site of the transition region. The best strategy is achieved by rate of twist variation, tapering it off to zero towards the fixed end of the spinal axis. This causes only a single transition region to nucleate, which is forced to travel along the spinal axis.

To understand the mechanism a two-dimensional link and slider model is proposed that explains the torque as a product of two types of springs. The first are linear springs inside the links, they simulate the bistable behaviour of the helicoid, as the result of the compression of a link. The revolute springs on the sliders, connecting the links, simulate the transition region. This model enables the helicoid to be entirely predicted by the geometry of the edge, simplifying the problem.

A analytical solution based on this link and slider model is presented that predicts the result of the numerical model, in order to create a design tool that allows for the rapid design of a tailored torque-twist helicoidal shell. This manual design strategy is much faster than numerical shape optimisation. This is due to the analytical solution being fast enough to have a live prediction for any alteration made, after which the numerical method is only used to verify the prediction. Using this method, a simple tailored curve could be designed in as little as 5 minutes, and subsequently verified numerically in an additional 15 minutes.

As a part of the analytical solution a Saint-Venant model is created that uses slices of equivalent constant rate of twist helicoidal shells in order to make a combined stiffness term. This model suffices for simple curves, but becomes progressively more inaccurate as more complex tailored curves are made. Therefore in the future the helicoidal stiffness model should be expanded, including the stiffening effects of the transition region.

A few examples of tailored torque-twist curves were designed and manufactured, among which a sinusoidal curve for a gravity balancer. In previous work by Abouheidari et al.[14], the cross section geometry was altered, and shape optimisation was used to achieve the same goal, successfully following the first 140° of a sinus. Using the rate of twist variation method, the first 150° could be designed, the limiting factor being the possible nucleation of a second transition region.

Further research into the manufacturing of the helicoidal shells should also be conducted, since experimental results, using PETG FDM printing have been inconsistent.

In this paper, the behaviour of the helicoidal shell is described by sampling a single point along the spinal axis, in reality the behaviour is affected by the entire transition region. As such, any further research should focus on understanding the formation and behaviour of the transition region. In the resulting model the radius and the shell thickness could also become usable design variables, likely expanding the possible design space that could be achieved. It would also allow for the improvement of the Saint-Venant Stiffness model presented in this paper, as it could model the stiffening effect of the transition region.

Finally, to further expand the applicability of the helicoidal shell, stress relaxation could be explored as a means to obtain a Tailored torque curve that can generate both positive as well as negative torque values. This would expand on the work of Blaakman et al. [20] where constant rate of twist helicoids were made neutrally stable using this principle.

*References*


[1] Larry L. Howell. *Compliant Mechanisms*. New York: John Wiley & Sons, 2001. ISBN: 9780471384786.

[2] Yilun Sun and Tim C. Lueth. "Safe Manipulation in Robotic Surgery Using Compliant Constant-Force Mechanism". In: *IEEE Transactions on Medical Robotics and Bionics* 5.3 (Aug. 2023), pp. 486–495. ISSN: 2576-3202. DOI: 10.1109/TMRB.2023.3237924.

[3] G. Radaelli and J. L. Herder. "Gravity balanced compliant shell mechanisms". In: *International Journal of Solids and Structures* 118-119 (2017), pp. 78–88. DOI: 10.1016/j.ijsolstr.2017.04.021.

[4] A. J. Lamers, J. A. Gallego Sánchez, and J. L. Herder. "Design of a statically balanced fully compliant grasper". In: *Mechanism and Machine Theory* 92 (2015), pp. 230–239. DOI: 10.1016/j.mechmachtheory.2015.05.014.

[5] Xiaozhi Zhang, Guangwei Wang, and Qingsong Xu. "Design, Analysis and Testing of a New Compliant Compound Constant-Force Mechanism". In: *Actuators* 7.4 (2018). DOI: 10.3390/act7040065.

[6] Guoqiang Chen and Shiguang Zhang. "Fully-compliant statically-balanced mechanisms without prestressing assembly: concepts and case studies". In: *Mechanics & Science* 2.2 (2011), pp. 169–174. DOI: 10.5194/ms-2-169-2011.

[7] Guangbo Hao, John Mullins, and Kevin Cronin. "Simplified modelling and development of a bi-directionally adjustable constant-force compliant gripper". In: *Proceedings of the Institution of Mechanical Engineers, Part C: Journal of Mechanical Engineering Science* 231.11 (June 2017), pp. 2110–2123. ISSN: 0954-4062. DOI: 10.1177/0954406216628557.

[8] Guimin Chen, Yanjie Gou, and Lei Yang. "Research on Multistable Compliant Mechanisms: The State of the Art". In: *Proceedings of the 9th International Conference on Frontiers of Design and Manufacturing (ICFDM)*. School of Mechatronics, Xidian University, Xi'an, China. Changsha, China, July 2010, pp. 1–5.

[9] Yanjie Gou, Guimin Chen, and Larry L. Howell. "A Design Approach to Fully Compliant Multistable Mechanisms Employing a Single Bistable Mechanism". In: *Mechanics Based Design of Structures and Machines* 49.7 (2021), pp. 986–1009. DOI: 10.1080/15397734.2019.1707685.

[10] Mohamed Zanaty et al. "Reconfigurable Logic Gates Based on Programmable Multistable Mechanisms". In: *Journal of Mechanisms and Robotics* 12.2 (2020), 021111–1–021111–? DOI: 10.1115/1.4045970.

[11] Tingting Ye et al. "A Novel Two-Stage Constant Force Compliant Microgripper". In: *Journal of Mechanical Design* 143.5 (May 2021). ISSN: 1050-0472. DOI: 10.1115/1.4048217.

[12] Maximillian D. X. Dixon et al. "Bespoke extensional elasticity through helical lattice systems". In: *Proceedings of the Royal Society A: Mathematical, Physical and Engineering Sciences* 475.2232 (Dec. 2019), p. 20190547. ISSN: 1364-5021. DOI: 10.1098/rspa.2019.0547.

[13] Giuseppe Radaelli. "Reverse-twisting of helicoidal shells to obtain neutrally stable linkage mechanisms". In: *International Journal of Mechanical Sciences* 202-203 (2021). ISSN: 00207403. DOI: 10.1016/j.ijmecsci.2021.106532.

[14] S. Abouheidari. "Synthesis of Nonlinear Torque-angle Profile Using Compliant Helicoidal Shell Joint". Master's thesis. Delft, The Netherlands: Delft University of Technology, 2024. DOI: https://resolver.tudelft.nl/uuid:71500cd9-d2e3-4c02-8aca-63edad0638b2.

[15] Attila P. Nagy, Samuel T. IJsselmuiden, and Mostafa M. Abdalla. "Isogeometric design of anisotropic shells: Optimal form and material distribution". In: *Computer Methods in Applied Mechanics and Engineering* 264 (Sept. 2013), pp. 145–162. ISSN: 00457825. DOI: 10.1016/j.cma.2013.05.019.

[16] Ultimaker B.V. *Ultimaker PETG Technical Data Sheet*. v5.00. Accessed: November 2025. Ultimaker B.V. Geldermalsen, The Netherlands, 2022. URL: https://www.dynamism.com/media/catalog/product/pdf/Ultimaker_PETG_TDS.pdf?.

[17] J. M. Mercado-Colmenero, A. Rubia, and A. Aragón. "Experimental and Numerical Analysis for the Mechanical Characterization of PETG (Polyethylene Terephthalate Glycol) Manufactured with FDM Technology under Pure Uniaxial Compression Stress States for Architectural Applications". In: *Polymers* 12.11 (2020), p. 2517. DOI: 10.3390/polym12112517. URL: https://www.ncbi.nlm.nih.gov/pmc/articles/PMC7600181/.

[18] C. R. Calladine. *Theory of Shell Structures*. Cambridge: Cambridge University Press, 1983. ISBN: 9780521233734.

[19] Jan Loskot et al. "Influence of print speed on the microstructure, morphology, and mechanical properties of 3D-printed PETG products". In: *Polymer Testing* 123 (2023), p. 108055. DOI: 10.1016/j.polymertesting.2023.108055.

[20] M. Blaakman. "Relax to stress". Master's thesis. Delft, The Netherlands: Delft University of Technology, 2024. DOI: https://resolver.tudelft.nl/uuid:421ec908-96b6-4634-a93c-fdb8ce325dbf.

## APPENDIX

### A. Constant Component Determination

The $\beta$ scaling simulations performed in the paper are expanded upon in this section. These tests are performed with a shell thickness of 0.4 and the PETG Young's Modulus of 2.1 GPa given by RealFilament, which is a rough estimate chosen before chosen before tests showed print orientation should be considered. But as the Young's Modulus scales linearly in the determined equation and FEM input the data was thus deemed usable.

These FEM simulations were performed in 70 steps, as this was the amount of elements before mesh refinement. It however strikes a decent balance between sampling density and simulation time. Each simulation took around 15 minutes.

The way the data was collected was simply to take the torque value at the same FEM step for every helicoid simulated. FEMstep 40 was chosen as for higher Radii it remained relatively unaffected by the entrance and end behaviour. This worked well for the first 7 radius increments as these had near perfect constant torque regions, though the highest two increments started to be dominated by entrance and end behaviour. This effect is clearly observed in the figures.

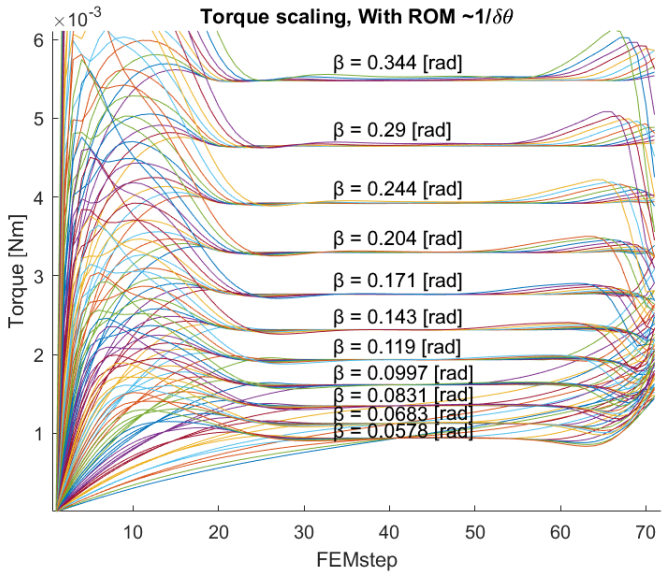


Fig. 19. Constant Torque Region scaling result from the scaling steps discussed in the main paper. It also visualises the lower parameter limits for which the transition region can nucleate. The x-axis shows the FEM steps as this is the data that the torque values are taken from. The data is taken from FEM step 40.

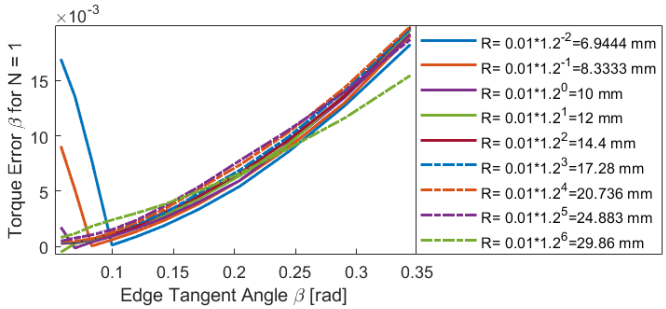


Fig. 20. Error of the $f_{\text{BS}} = \beta$ prediction for constant torque curves. The peaks at the lower $\beta$ values are due to the helicoid not being able to form a transition region as can be observed in Fig.19.

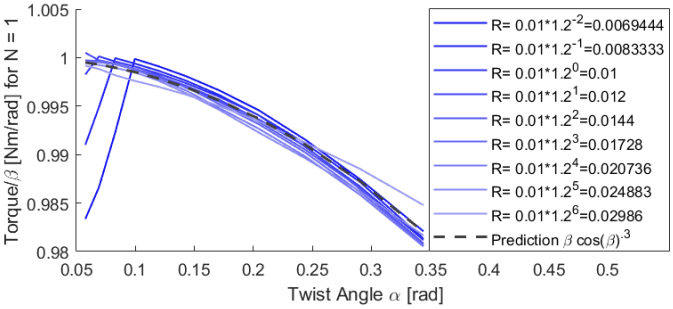


Fig. 21. The torque divided by the prediction using $f_{\text{BS}} = 2\beta$. It also shows the $\cos(\beta)^{\cdot 3}$ component. The dips for lower values of $\alpha$ are due to the transition region not being able to form as shown in Fig. 19

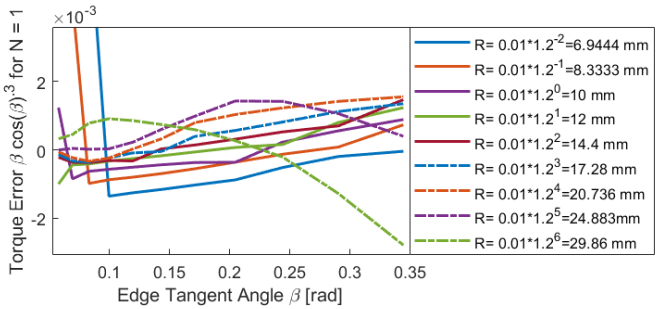


Fig. 22. Graph showing the torque error of the $f_{\text{BS}} = 2\beta cos(\beta)^{\cdot 3}$ constant torque prediction.

### B. Bezier Transition Region Prediction

The shape of the transition region can be approximated using a cubic bezier curve, whose two central control points are crossed. The extension beyond their crossing point can be determined using a optimisation algorithm that compared the arclength of the Beziercurve to the length of the straight lines up to the crossing point. This yields an extension factor $o$.

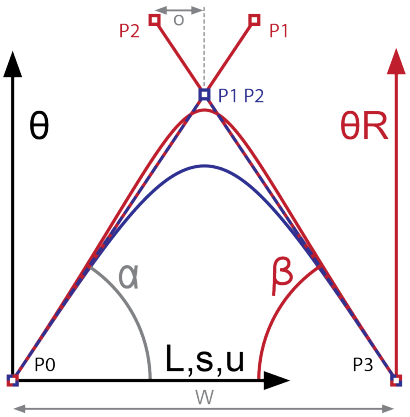


Fig. 23. The representative cubic Bezier curve visualised, where the red is the edge curve, created by pulling the middle two control points beyond the intersection. Blue represents an ideal case where the spine does not follow the edge. This curve has both its two middle control points on the intersection. The black is the difference between the two lines, and this represents $\Gamma$ the total in-slice deflection angle. The black $\theta$ axis corresponds rotation of the curve around the spine and applies to all the curves to the $\alpha$ angle, whilst the red $\theta R$ axis corresponds to the geometry of the edge if rolled out, and only corresponds to the red edge curve, as well as $\beta$.

This prediction method is far from perfect, but it could be practical if a complete analytical transition region bending model cannot be set up. The main obstacle of the Bezier model lies in the area it is designed to solve: The differential behaviour. The issue lies in the straight nature of the lines of the control points. Which ideally would be curved, if one is to actually vary the rate of twist. It therefore remains uncertain how the bezier prediction should be influenced by its surrounding geometric values, though the following option could be promising.

A possible method to make the bezier model responsive to a variable rate of twist input, is to use the curvature curve as an influence window. Similar to a normal distribution, the total area could be normalised. Subsequently, for each side a weighted average, according to local height on the curvature plot, could be used as an input. The responses of the Bezier model to a symmetric and a asymmetric rate of twist input are shown in Fig. 24 and Fig. 25, where the latter has a right side rate of twist input of twice that of the left side.

For a constant rate of twist curve, with a shell thickness of 0.4 mm, the distance between the outer control points $W$ can be approximated as $3.5R$. This value, however, is only an initial estimate that seems to hold for the curves made in this paper. Further study to investigate the range of applicability should be performed if it is to be used more extensively.

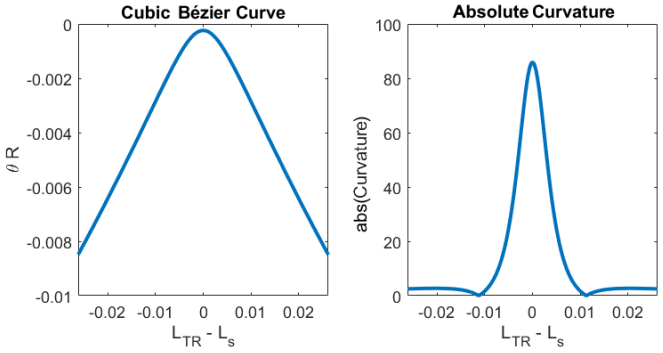


Fig. 24. The transition region shape and curvature prediction of a constant rate of twist helicoidal shell. $R$ = 15 mm, $\alpha_{\text{left}} = \alpha_{\text{right}}$ = 21.5 rad/mm.

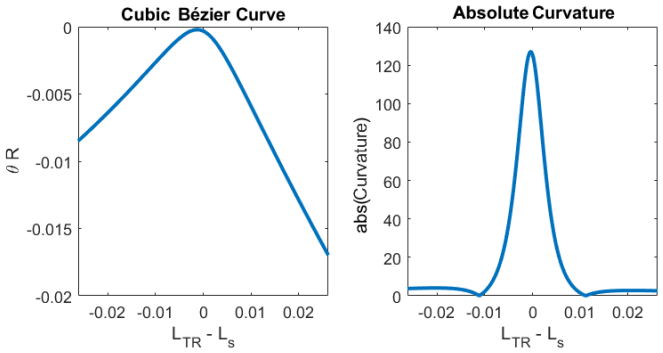


Fig. 25. The transition region shape and curvature prediction of an extreme example where the right side has twice the rate of twist as the left. Comparing this prediction to that in Fig. 24, a shift towards the left is observed. $R$ = 15 mm, $\alpha_{\text{left}}$ = 21.5 rad/mm, $\alpha_{\text{right}}$ = 43 rad/mm

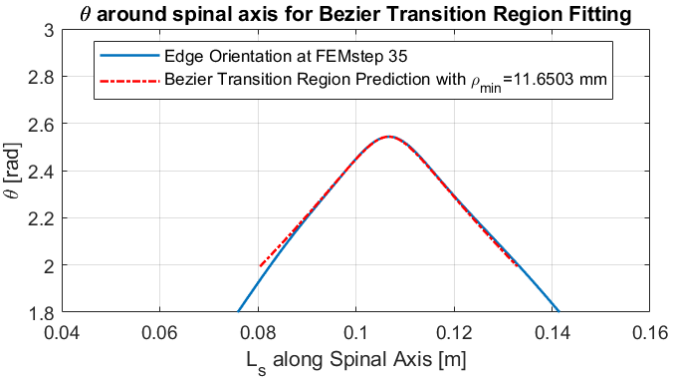


Fig. 26. An example of a transition region prediction by a bezier curve, using a constant rate of twist input. It shows a good overlap for the central part of the prediction, but it become worse once the curvature becomes negative

The equations for the x and y components of the cubic bezier curve used are given by the following equations [1]:

TABLE II
CONTROL POINTS FOR THE BEZIER TRANSITION REGION PREDICTION, WHERE $W$ IS THE DISTANCE BETWEEN THE CONTROL POINTS, $o$ IS THE OPTIMISED FACTOR THAT THE MIDDLE CONTROL POINTS EXTEND FROM THE ORIGIN. $l$ AND $r$ REFER TO THE SIDE FROM THE ORIGIN THAT THE VARIABLE IS SAMPLED FROM.

| Point | $P_x$ | $P_y$ |
|---|---|---|
| $P_0$ | $-W/2$ | -$\alpha_l RW/2$ |
| $P_1$ | $o_L$ | $o_l \alpha_r R$ |
| $P_2$ | $-o_R$ | $o_l \alpha_l R$ |
| $P_3$ | $W/2$ | $-\alpha_r RW/2$ |

$$Bx_u = (1-u)^3 P_{0x} + 3(1-u)^2 u P_{1x} + 3(1-u)u^2 P_{2x} + u^3 P_{3x} \tag{23}$$

$$By_u = (1-u)^3 P_{0y} + 3(1-u)^2 u P_{1y} + 3(1-u)u^2 P_{2y} + u^3 P_{3y} \tag{24}$$

Where $u$ the bezier coordinate between 0 and 1. The radius of curvature is obtained by differentiating multiplication of the derivatives of $Bx$ and $By$, divided by the magnitude cubed.

$$\frac{1}{\rho_{s,u}} = \kappa_{\text{Bezier},s,u} = (Bx'_u By''_u - By'_u Bx''_u)/(Bx_u^2 + By_u^2)^{\frac{3}{2}} \tag{25}$$

Where $\kappa_{\text{Bezier}}$ and $\rho$ are the of curvature and the radius curvature of the Bezier curve.

*References*


[1] Pomax. *A Primer on Bézier Curves*. https://pomax.github.io/BezierInfo-2/. Accessed: November 2025. 2025.

### C. Radius and Thickness Variation

As the initial goal of this work was to eventually investigate all three design variables, a preliminary test is performed. In this test, all three variables are given the same variation input, namely the addition of a single sinusoidal peak, with a peak to peak height of 4% of the constant input value as shown in Fig. 27. The base helicoid had the following parameters: rate of twist $\alpha$: 20 rad/m, thickness t: 0.4 mm and radius R:15 mm. For these tests an older version of the design code is used, as easily it allows for manual addition of a variation by means of list addition. The resulting torque-twist curves are are shown in Fig. 28.

From this test a few observations can be made. Thickness variation is mostly a result of the undifferentiated term, as the dip following the peak is small. Rate of Twist variation is, as shown repeatedly a product of both the undifferentiated term as well as the first derivative. Radius variation gives a more interesting result. It is clearly also driven, besides the undifferentiated and the first derivative term, by the second derivative of the radius.

This implies that it could be possible, once their exact workings are known, that an approach that uses all three variables could improve the control on a resulting torque curve. An example being that perhaps an undesirable dip from a rate of twist down step could be balanced out by a local increase of the thickness. This idea is shown in Fig. 29. It both shows the individual variation results as well as the result of when they are combined.

Whilst thickness variation might seem straight forward, it cannot be predicted with the point model used in the paper. This stems from the emergent behaviour occurring earlier in the rotation than expected. This difference in behaviour is visualised in Fig. 29. Saint-Venant stiffness effects, though unmodelled for thickness variation, should not result in this big of a difference as can be seen from Fig. 28 where the entrance and end behaviour remain virtually unchanged between the different variation types. Part of this can be explained by the relatively small derivative component dragging the peak forwards, but thickness variation has on the whole a wider range of effect than rate of twist variation does. As such the predictions could be helped by the introduction of a transition region model, that is affected by a wider area than just a point.

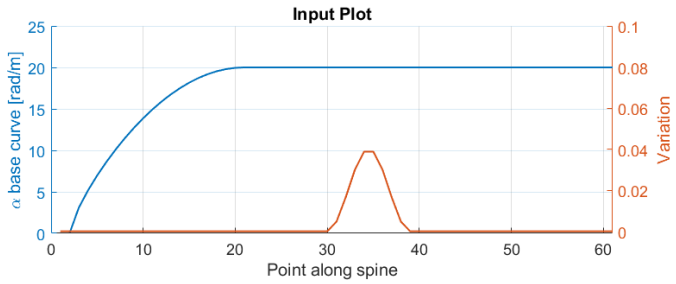


Fig. 27. Inputs of the rate of twist base curve in blue, and the added variation used in Fig 28. As input only 60 points are used which are smoothened using NURBS before being used in the numerical model.

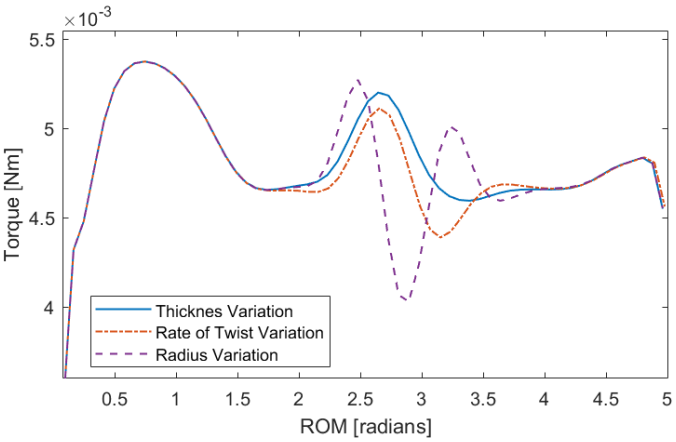


Fig. 28. The numerical results of the same thickness, rate of twist, and radius variation input on the resulting torque-twist curve. All three helicoids have the same constant rate of twist helicoid, with a nucleation region, as a basis.

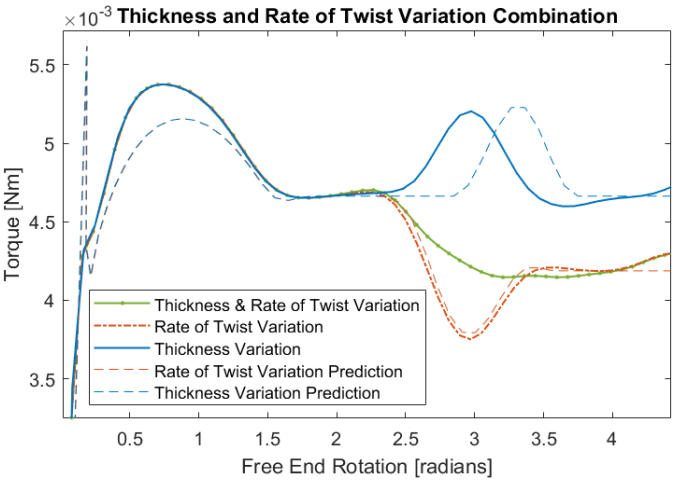


Fig. 29. The numerical result of combined thickness and rate of twist variation in order to counteract the dip in a rate of twist decrease. The individual variations are also shown. The dashed curves show the predicted results. From these it can be observed that the thickness point prediction results in a large offset, whereas the point prediction of the rate of twist follows the curve well. For the predictions an earlier prediction model is used, as it allows for variation to the variables along the spine length, by means of list summation. This explains the initial peak, as well as the worse rate of twist prediction than shown in the rest of this work.

### D. Saint-Venant Torsional Stiffness

The Saint-Venant stiffness term is the rotational stiffness of the helicoid if no transition region is nucleated. The easiest way it can be observed is to twist the helicoid in the same direction as its twist, thus tensioning the helicoid. The value of the Saint-Venant stiffness term is, within small deflections, assumed to be the same in either direction of twist. And thus present when the helicoid is reverse twisted. It therefore needs to be added to the prediction model.

#### 1) Slice Stiffness Lookup-Table Model

As no sufficient stiffness model was made, nor found, to approximate the Saint-Venant torsion stiffness of the helicoid, a lookup table was generated. With this lookup table a composite stiffness is formed, using for every slice the stiffness of an equivalent helicoid. These slices are them combined into a total stiffness of the designed helicoid, a simplified version of which is shown in Fig. 30

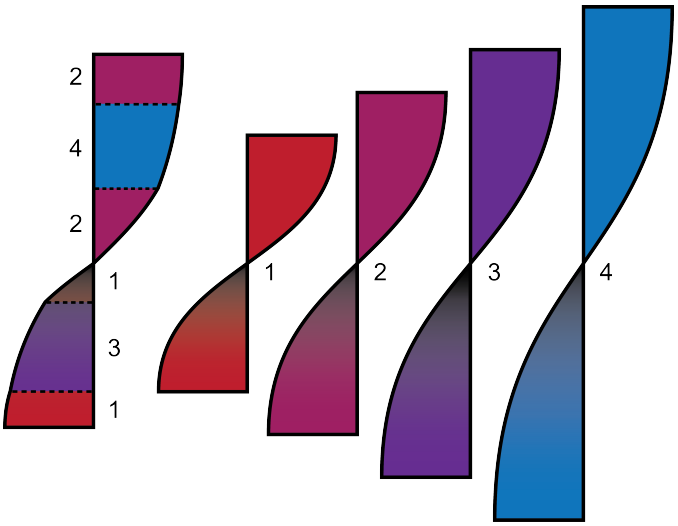


Fig. 30. Visualisation of the composite stiffness model, where the variable rate of twist helicoid on the left is a composite of equivalent helicoids with varying Rates of Twist on the right, as denoted by the colour as well as the number.

The data for this lookup table is collected by numerical simulations where a range of constant rate of twist helicoids is twisted in the direction of geometrical twist. This range was iterated within a rate of twist range of 0-60 rad/m and a radius range of 2-20 mm. For the The thickness the value of 0.4 mm is used this is the value used in the paper. In order to minimise the boundary effects, the length was set to 150 mm. Further steps included the lowering of the rotational constraint strength on the end points as well as stiffening the positional constraints. Each helicoid was twisted 0.01 radians. Finally the edge behaviour was isolated by only observing the twist of a central length fraction of the helicoid. From these results the polar moment of intertias J are determined using the following formula[1]:

$$J = \frac{Tl}{\theta G} \tag{26}$$

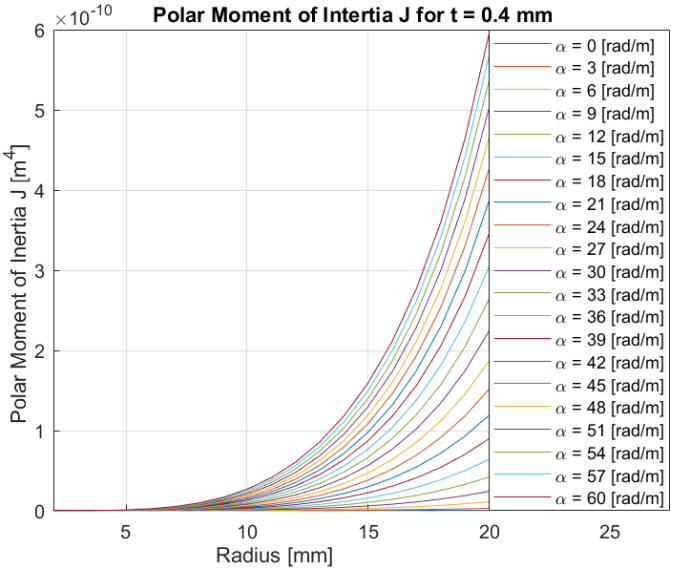


Fig. 31. Polar Moment of Intertia J determined with thickness = 0.4 mm.

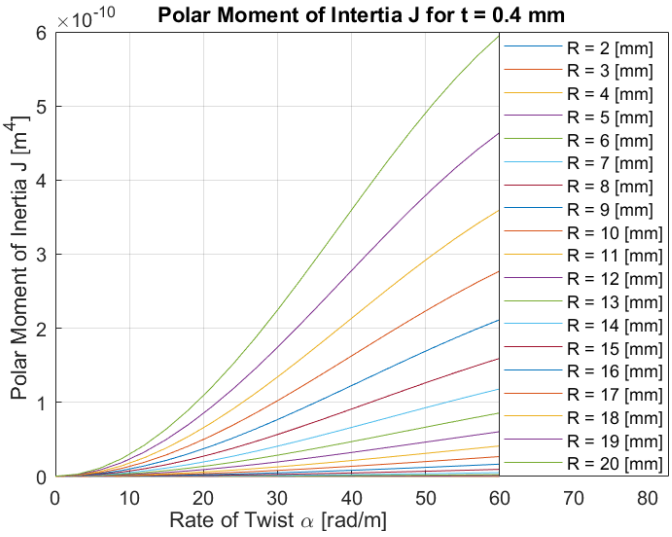


Fig. 32. Polar Moment of Intertia J determined with thickness = 0.4 mm.

The resulting J values are plotted in Fig. 32 and Fig. 31 and tabulated in Table. IV and Table. V.

This model does not account for more emergent effects such as the effect that differing adjacent rates of twist have on warping. As such errors are to be expected. A second source of error is that the effect of the transition region is not modelled. The forced shape of the transition region is expected to have a stiffening effect within its area. Lastly, the model avoids the effect of the edge

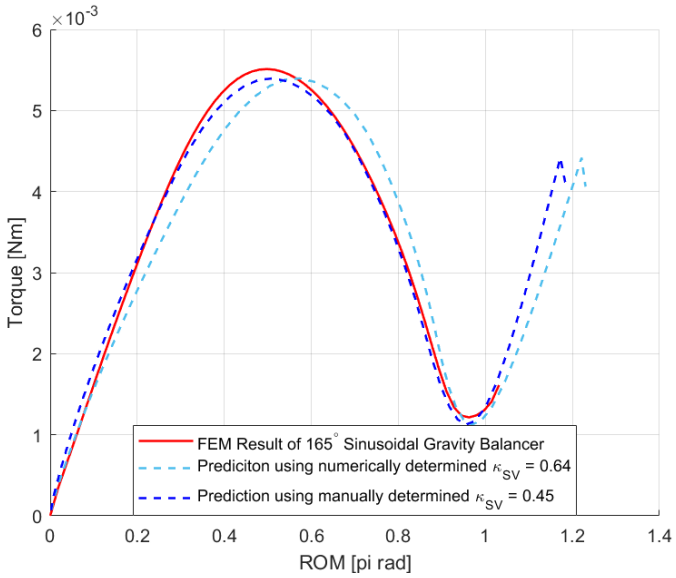


Fig. 33. FEM result of the sinusoidal curve with two analytical predictions with differing stiffness correction factors $\kappa_{SV}$. Where the dark blue line is the generally applicable guess of $\kappa_{SV}$= 0.45, and the light blue line is that of the numerically determined $\kappa_{SV}$= 0.64.

In order to correct for these effects a torsional stiffness correction factor $\kappa_{SV}$ is added. The warping effect error can be determined with the same method as is used for the Lookup Table. If this correction factor is then applied, as shown tested in Fig. 33 for the 180° sinusoidal gravity balancer, the resulting prediction is, excluding the beginning, too compliant. This is supposed to be due to the transition region stiffening effect. Instead, it was determined that using an initial guess of $\kappa_{SV}$ = 0.5 a much better overall prediction could be made, for most curves. This can then be refined after the first FEM validation cycle. In this manner the designed curves used values for $\kappa_{SV}$ as show in Tab. III The resulting solution for twist, as the transition regions reaches slice $s$, therefore becomes:

TABLE III
$\kappa_{SV}$ USED FOR THE TAILORED CURVES DISCUSSED IN THE PAPER.

| Tailored Curve | Lin. Decrease | Lin. Increase | 165° Sinus | 360° Sinus |
|---|---|---|---|---|
| $\kappa_{SV}$ *Manual* | 0.7 | 0.7 | 0.45 | 0.7 |

$$\theta_s = 2\phi_s + \theta_{SVs} \tag{27}$$

with $\theta_{SV}$ being the Saint-Venant deflection defined as follows.

$$\theta_{SVs} = T_s/K_{SV} = \frac{T_s \kappa_{SV}}{G} \sum_{s=0}^{s=L} \frac{l_s}{J_s} \tag{28}$$

*References*

[1] Warren C. Young, Richard G. Budynas, and Ali M. Sadegh. *Roark's Formulas for Stress and Strain*. 9th ed. New York: McGraw-Hill, 2012. ISBN: 978-0071742474.

TABLE IV

VALUES FOR POLAR MOMENT OF INERTIA J $\cdot 10^{11}$ FOR SHELL THICKNESS = 0.4 MM. UNITS FOR $\alpha$ ARE RAD/M, WHILST THOSE FOR RADIUS ARE IN MM.

| $\alpha$ \Radius | 3 | 4.5 | 6 | 7.5 | 9 | 10.5 | 12 | 13.5 | 15 | 16.5 |
|---|---|---|---|---|---|---|---|---|---|---|
| 0 | 0.0042 | 0.0062 | 0.0083 | 0.0104 | 0.0125 | 0.0146 | 0.0166 | 0.0187 | 0.0208 | 0.0229 |
| 3 | 0.0042 | 0.0063 | 0.0084 | 0.0107 | 0.0131 | 0.0159 | 0.0193 | 0.0236 | 0.0291 | 0.0362 |
| 6 | 0.0042 | 0.0063 | 0.0087 | 0.0114 | 0.0151 | 0.0202 | 0.0277 | 0.0386 | 0.0545 | 0.0771 |
| 9 | 0.0042 | 0.0064 | 0.0091 | 0.0128 | 0.0184 | 0.0273 | 0.0415 | 0.0636 | 0.0968 | 0.1451 |
| 12 | 0.0042 | 0.0066 | 0.0097 | 0.0146 | 0.0230 | 0.0373 | 0.0609 | 0.0984 | 0.1556 | 0.2396 |
| 15 | 0.0042 | 0.0067 | 0.0105 | 0.0170 | 0.0289 | 0.0500 | 0.0857 | 0.1429 | 0.2306 | 0.3597 |
| 18 | 0.0043 | 0.0070 | 0.0114 | 0.0199 | 0.0361 | 0.0655 | 0.1157 | 0.1967 | 0.3210 | 0.5042 |
| 21 | 0.0043 | 0.0072 | 0.0125 | 0.0233 | 0.0445 | 0.0836 | 0.1508 | 0.2594 | 0.4262 | 0.6717 |
| 24 | 0.0043 | 0.0075 | 0.0138 | 0.0272 | 0.0542 | 0.1044 | 0.1909 | 0.3308 | 0.5454 | 0.8608 |
| 27 | 0.0044 | 0.0079 | 0.0153 | 0.0316 | 0.0651 | 0.1277 | 0.2357 | 0.4103 | 0.6777 | 1.0698 |
| 30 | 0.0044 | 0.0083 | 0.0169 | 0.0365 | 0.0772 | 0.1534 | 0.2851 | 0.4975 | 0.8222 | 1.2967 |
| 33 | 0.0045 | 0.0087 | 0.0186 | 0.0419 | 0.0904 | 0.1815 | 0.3387 | 0.5918 | 0.9776 | 1.5398 |
| 36 | 0.0045 | 0.0091 | 0.0206 | 0.0477 | 0.1047 | 0.2118 | 0.3963 | 0.6927 | 1.1431 | 1.7969 |
| 39 | 0.0046 | 0.0096 | 0.0227 | 0.0540 | 0.1201 | 0.2443 | 0.4577 | 0.7997 | 1.3175 | 2.0661 |
| 42 | 0.0047 | 0.0102 | 0.0249 | 0.0608 | 0.1365 | 0.2787 | 0.5226 | 0.9121 | 1.4995 | 2.3454 |
| 45 | 0.0047 | 0.0107 | 0.0273 | 0.0680 | 0.1539 | 0.3151 | 0.5907 | 1.0293 | 1.6882 | 2.6326 |
| 48 | 0.0048 | 0.0114 | 0.0299 | 0.0756 | 0.1723 | 0.3532 | 0.6617 | 1.1507 | 1.8822 | 2.9258 |
| 51 | 0.0049 | 0.0120 | 0.0326 | 0.0836 | 0.1915 | 0.3930 | 0.7353 | 1.2757 | 2.0804 | 3.2231 |
| 54 | 0.0050 | 0.0127 | 0.0354 | 0.0920 | 0.2116 | 0.4342 | 0.8112 | 1.4037 | 2.2819 | 3.5226 |
| 57 | 0.0048 | 0.0296 | 0.1077 | 0.2681 | 0.5020 | 0.7569 | 0.9753 | 1.1335 | 1.2383 | 1.3054 |
| 60 | 0.0052 | 0.0142 | 0.0415 | 0.1100 | 0.2540 | 0.5207 | 0.9686 | 1.6662 | 2.6898 | 4.1157 |

TABLE V

VALUES FOR POLAR MOMENT OF INERTIA J $\cdot 10^{11}$ FOR SHELL THICKNESS = 0.4 MM. UNITS FOR $\alpha$ ARE RAD/M, WHILST THOSE FOR RADIUS ARE IN MM.

| $\alpha$ \Radius | 18 | 19.5 | 21 | 22.5 | 24 | 25.5 | 27 | 28.5 | 30 |
|---|---|---|---|---|---|---|---|---|---|
| 0 | 0.0250 | 0.0271 | 0.0291 | 0.0312 | 0.0333 | 0.0354 | 0.0375 | 0.0396 | 0.0418 |
| 3 | 0.0456 | 0.0578 | 0.0737 | 0.0942 | 0.1202 | 0.1531 | 0.1941 | 0.2448 | 0.3068 |
| 6 | 0.0456 | 0.0578 | 0.0737 | 0.0942 | 0.1202 | 0.1531 | 0.1941 | 0.2448 | 0.3068 |
| 9 | 0.2137 | 0.3083 | 0.4361 | 0.6050 | 0.8243 | 1.1045 | 1.4570 | 1.8945 | 2.4307 |
| 12 | 0.3592 | 0.5247 | 0.7481 | 1.0436 | 1.4267 | 1.9152 | 2.5283 | 3.2869 | 4.2135 |
| 15 | 0.5436 | 0.7981 | 1.1414 | 1.5944 | 2.1807 | 2.9262 | 3.8594 | 5.0118 | 6.4194 |
| 18 | 0.7649 | 1.1250 | 1.6098 | 2.2479 | 3.0712 | 4.1151 | 5.4194 | 7.0299 | 9.0022 |
| 21 | 1.0205 | 1.5012 | 2.1465 | 2.9932 | 4.0825 | 5.4606 | 7.1811 | 9.3096 | 11.9290 |
| 24 | 1.3078 | 1.9220 | 2.7440 | 3.8191 | 5.1986 | 6.9415 | 9.1196 | 11.8235 | 15.1713 |
| 27 | 1.6237 | 2.3825 | 3.3943 | 4.7138 | 6.4033 | 8.5374 | 11.2098 | 14.5422 | 18.6954 |
| 30 | 1.9651 | 2.8772 | 4.0894 | 5.6655 | 7.6806 | 10.2275 | 13.4254 | 17.4320 | 22.4574 |
| 33 | 2.3285 | 3.4008 | 4.8209 | 6.6625 | 9.0149 | 11.9909 | 15.7384 | 20.4546 | 26.4036 |
| 36 | 2.7106 | 3.9480 | 5.5809 | 7.6937 | 10.3907 | 13.8065 | 18.1192 | 23.5677 | 30.4721 |
| 39 | 3.1081 | 4.5133 | 6.3615 | 8.7480 | 11.7928 | 15.6527 | 20.5370 | 26.7260 | 34.5960 |
| 42 | 3.5174 | 5.0916 | 7.1554 | 9.8149 | 13.2061 | 17.5082 | 22.9603 | 29.8829 | 38.7053 |
| 45 | 3.9354 | 5.6780 | 7.9552 | 10.8841 | 14.6160 | 19.3514 | 25.3576 | 32.9916 | 42.7308 |
| 48 | 4.3588 | 6.2677 | 8.7542 | 11.9458 | 16.0085 | 21.1620 | 27.6987 | 36.0075 | 46.6061 |
| 51 | 4.7847 | 6.8562 | 9.5460 | 12.9910 | 17.3704 | 22.9207 | 29.9554 | 38.8892 | 50.2714 |
| 54 | 5.2102 | 7.4394 | 10.3246 | 14.0112 | 18.6895 | 24.6099 | 32.1023 | 41.6006 | 53.6752 |
| 57 | 5.6326 | 8.0136 | 11.0848 | 14.9988 | 19.9550 | 26.2142 | 34.1178 | 44.1115 | 56.7764 |
| 60 | 6.0417 | 8.5645 | 11.8069 | 15.9253 | 21.1222 | 27.6605 | 35.8804 | 46.2219 | 59.2538 |

### E. Material Choice and Manufacturing

Before ultimately settling for PETG Fused Deposition Modeling (FDM), multiple materials and production methods were investigated to manufacture the helicoidal shells. This chapter lays out the overall findings on these production methods and presents test results that illustrate these findings.

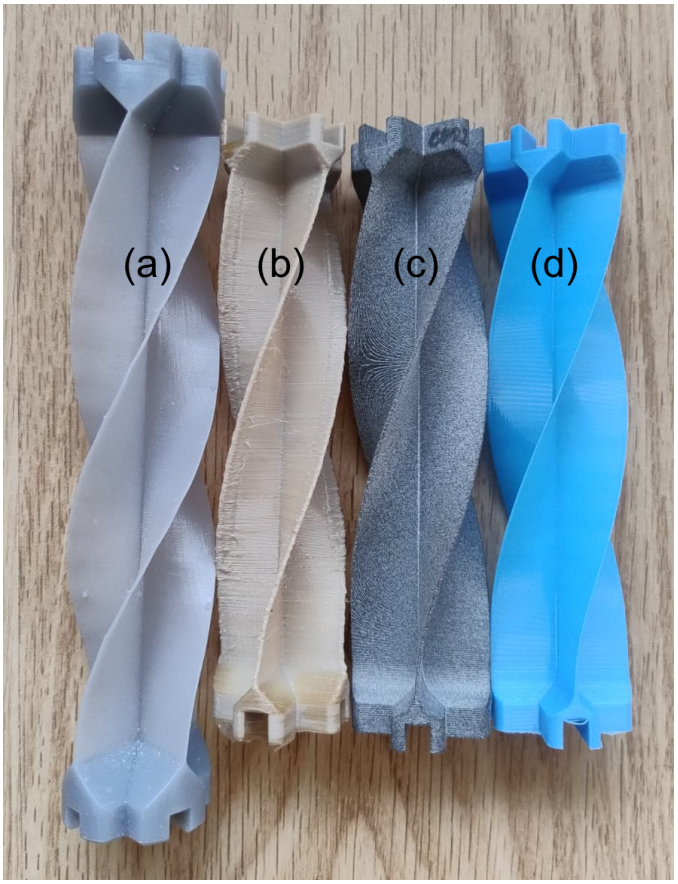


Fig. 34. Examples of the helicoids produced with different materials. (a) Tough 1500 SLA, (b) PEEK FDM, (c) Nylon Multi-Jet Fusion, (d) PETG FDM.

#### 1) PETG FDM

Initial tests were done with PETG FDM using an Ender 3 Pro. Here PETG was chosen as the filament has a low viscosity, and relatively interlayer adhesion. The latter of which is especially important as the shells are bent across the layer lines. For PETG FDM, the most important things to take into account to avoid the helicoid breaking are the shell thickness, and the print speed. The first as the forces scale by $t^3$ whilst the area only scales by $t$, the second as due to as of yet unknown reasons, a slower print speed results in more brittle helicoids. A slower print speed can however be advised when printing the upper end effector as it can sometimes fail, possibly due to some resonance effects.

#### 2) Tough 1500 SLA

Printing Tough 1500 [1] using SLA proves to not be suitable for the production of helicoids due to two mains issues. The first issue is that for higher radius or $\beta$ prints the shell sags in-between the supports, which can be clearly observed in Fig. 34(a). The second issue is that the material has a large amount of hysteresis, often dipping to negative torque values on the return stroke.

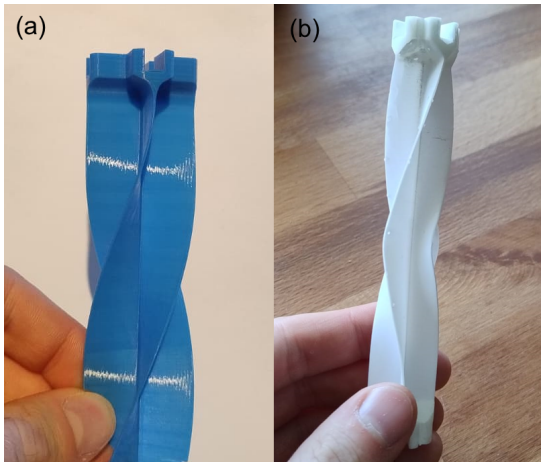


Fig. 35. (a) shows the layerthickness inconsistencies of the t = 0.4 mm PETG FDM helicoids, which are distinguishable as darker horizontal lines. (b) A Rigid 10K SLA helicoid twisted half its ROM, and then released.

#### 3) Rigid 10k SLA and PEEK FDM

The samples produced by Rigid 10k SLA [2] were never tested in the torsionbench as they are too brittle, requiring extreme care to twist. Once twisted however, it shows a remarkable behaviour in that it remains there, and requires almost the same torque to twist it back. The helicoid in its neutral rest position is shown in Fig. 35. The PEEK FDM samples produced had terrible interlayer adhesion, as well as having inconsistent layers, and is therefore best avoided in future production.

#### 4) Nylon Multi-Jet Fusion Powderbed

Following the example set by Radaelli [3] Nylon Multi-Jet Fusion [4] was initially decided to be used for the final tests. Whilst the resulting Torque-Twist curves are smoother and the helicoids not prone to breaking this does come at the cost of higher hysteresis. The produced helicoids had a shell thickness of 0.6 mm, which could exceed the thin walled assumptions for the smaller helicoids. This could be the reason for the $\beta$ scaling results shown in Fig. 36, where neither the radius nor the rate of twist scaling yielded the expected result. The radius scaling steps yielded much higher values than expected, the first step, averaging the forward and backward stroke, scaling with roughly 1.6 and the second with 1.4, which is much more than the predicted steps of roughly 1.2. The results of the $\alpha$ scaling steps yielded a first step scaling of roughly 0.75, and a second scaling step of 1.1. A similar 180° sinusoidal gravity balancer was made with Nylon, as was made with PETG. The experimental

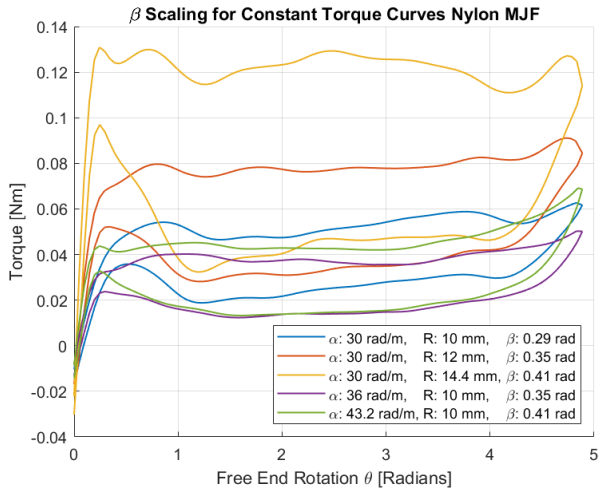


Fig. 36. $\beta$ scaling plots of the Nylon MJF 0.6 mm shell thickness helicoids. Just as with the PETG 0.6 mm thickness helicoids the torque does not follow the expected scaling. The radius scaling results yielding much higher values than expected, whilst the $\alpha$ scaling results decreasing the resulting torque. For each averaged curve two helicoids were twisted three times

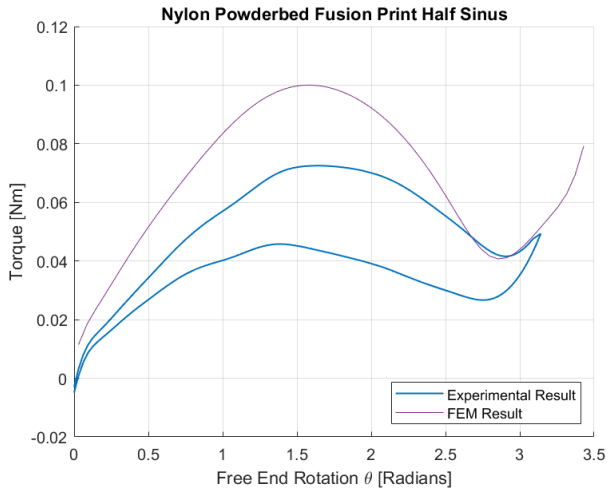


Fig. 37. Experimental result for the 180° Sinusoidal gravity balancer, made using Nylon MJF.

measurement is shown in Fig. 37, which shows that, similarly to the PETG version, the resulting torque is much lower than expected.

*5) Return to PETG FDM and shell thickness effect verification* In order to be able to iterate more effectively, the decision was made to return to PETG FDM using a Bambu Lab printer. Furthermore, the shell thickness for the paper was decreased to 0.4 mm, to avoid possibly exceeding the thickness for the thin-walled assumptions.

In order to investigate if the 0.6 mm shell thickness, rather Nylon as a material, caused the unexpected $\beta$ scaling behaviour, a few constant rate of twist helicoids were made The experimental results of that test are shown in Fig. 38. The results, whilst superficially similar, are different. The rate of twist scaling step, similarly to the Nylon result, does not increase, instead scaling by 0.97. The radius scaling, adheres to the expected scaling of 1.2. The difference between the two scaling results could indicate them being on the edge of the validity of the thin-walled behaviour.

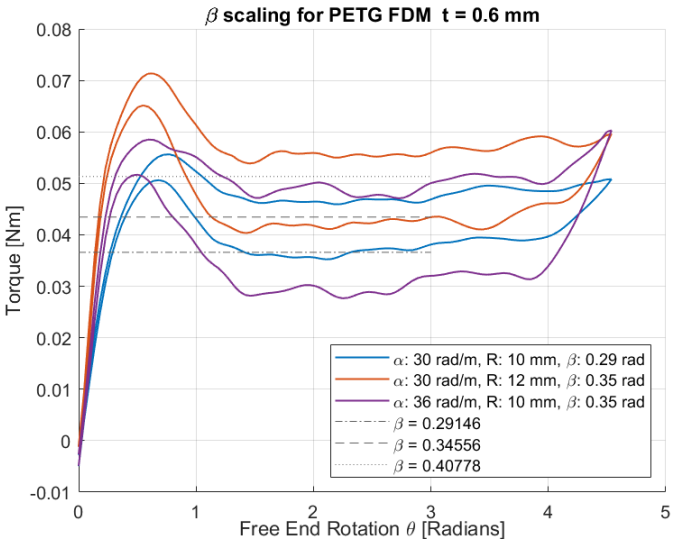


Fig. 38. $\beta$ scaling for PETG FDM 0.6 mm helicoids. For each averaged curve a single helicoid was twisted three times.

*References*


[1] Inc. Formlabs. *Tough 1500 Resin – Technical Data Sheet*. https://media.formlabs.com/m/32012de9e1a6dfbc/original/-ENUS-Tough-1500-TDS.pdf. Accessed: November 2025. 2020.

[2] Inc. Formlabs. *Rigid 10K Resin – Technical Data Sheet*. https://formlabs-media.formlabs.com/datasheets/2001479-TDS-ENUS-0.pdf. Accessed: November 2025. 2020.

[3] Giuseppe Radaelli. "Reverse-twisting of helicoidal shells to obtain neutrally stable linkage mechanisms". In: *International Journal of Mechanical Sciences* 202-203 (2021). ISSN: 00207403. DOI: 10.1016/j.ijmecsci.2021.106532.

[4] Materialise NV. *Multi Jet Fusion – Materialise Datasheets*. https://assets-eu-01.kc-usercontent.com/8ff24b0e-57a3-0157-62d1-fa4ac9734eb5/3b5bc854-7229-4c44-b4e8-9d198ea57ad7/materialise-datasheets-multi-jet-fusion.pdf. Accessed: November 2025. 2023.

### F. Shell Thickness Experiments

#### 1) Shell Thickness Tests

Initial tests with PETG FDM resulted in torque curves that were much lower than predicted. In order to find the cause for this difference a few 3-point bending tests are performed. These tests are also performed to determine overhang angle of a printed strip had an effect on the stiffness. In order to avoid environmental differences between samples, all strips are printed within the same batch. These samples come in two series, one with a shell thickness of 0.4 mm and one for a thickness of 0.6 mm. Each series consists of five strips, with a width of 10 mm, a length of 40 mm and with the following overhang angles: 0°, 5°,10°, 20°, and 30°. In retrospect a further 40° should also have been tested, in order to inspect if the change at 30° continues for higher values. Of each strip a thickness measurement is taken in order to determine the thickness error of the printer, these values are shown in Table VI. They show a relatively linear behaviour up until the 30°, where both thicknesses show a jump. The results of the 3-Point bending tests are shown in FIG. 39.

TABLE VI
MEASURED THICKNESSES OF 3-POINT BENDING TEST STRIPS IN MM.

| angle | 0° | 5° | 10° | 20° | 30° |
|---|---|---|---|---|---|
| t = 0.4 mm | 0.43 | 0.42 | 0.42 | 0.41 | 0.45 |
| t = 0.6 mm | 0.58 | 0.58 | 0.59 | 0.61 | 0.58 |

For the shell thickness of 0.4 mm, the sample with an overhang angle of 30° yields higher force values. This can be explained by the jump in measured thickness shown in Table VI. In order to illustrate this, the equation for the three point bending test is inspected[1]:

$$E_f = \frac{L^3}{4wt^3}\frac{F}{\delta} \tag{29}$$

The equation shows that the force scales with $t^3$. This leads to Fig. 40(a), where the force is divided by $t^3$. It shows that most of the the thickness normalised samples largely group together.

The tests on the 0.6 mm, however, show a different behaviour. For the force measurement in Fig. 39(b) two distinct groups can be observed, those printed at a lower angle than 20° and those at or above. This difference is subsequently not resolved when the force is divided by $t^3$ in Fig. 40(b). Whilst this points to large inconsistencies that could have caused the difference between the scaling steps for the 0.6 mm thick helicoids, no direct conclusion can be made as any $\beta$ scaled helicoid has, by definition, the same outer overhang angle, and would therefore be expected to have the same percentage of error.

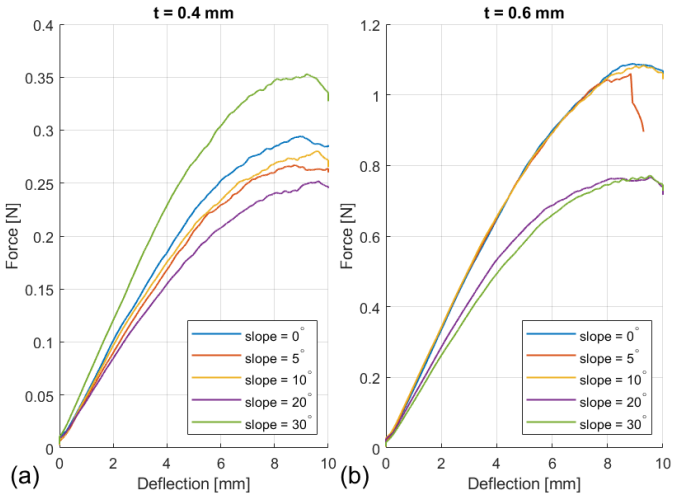


Fig. 39. Three-Point bending tests of PETG FDM sampled, printed under increasing overhang angles. (a) shows the data for tests with a shell thickness of 0.4 mm, whilst (b) shows those with a thickness of 0.6 mm.

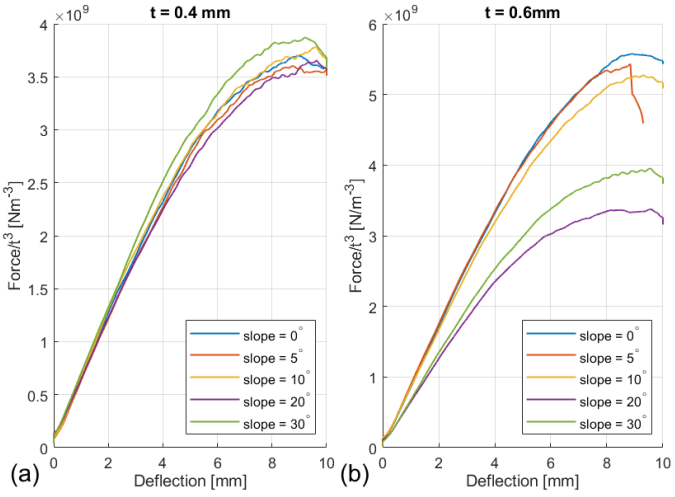


Fig. 40. Three-Point bending tests of PETG FDM sampled, printed under increasing overhang angles. The force of the three-point bending tests divided by the measured thickness of the corresponding sample. (a) shows the data for tests with a shell thickness of 0.4 mm, whilst (b) shows those with a thickness of 0.6 mm.

### References


[1] C. C Wang C. Sun. "A critical examination of three-point bending for determining Young's modulus". In: *International Journal of Pharmaceutics* 629 (2022), p. 122409. DOI: https://doi.org/10.1016/j.ijpharm.2022.122409.

### G. Non-linearly Elastic Effects

The FEM model assumes a linearly elastic material. Whilst this assumption is correct for low strain applications, the helicoidal shells might exceed its applicability. This possibility is investigated in the following section.

The way chosen to investigate the elastic regime is to calculate the strain in the edge of the helicoidal shell. Gere [1] gives the strain due to bending as:

$$\epsilon = -\frac{y}{\rho}, \quad abs(\epsilon_{\max}) = \frac{t}{2\rho} \tag{30}$$

Where y is the thickness coordinate from the shell centreline and $\rho$ is the radius of curvature. From this the highest value for can be determined at coordinate $y = t/2$, as shown subsequently.

Using the three point bending tests performed in Appendix F, we can determine the elastic regime of a specific strain. Here it is assumed that whilst the test yields an unusable Young's Modulus, that the elastic regimes with respect to the deflection are representative. From Fig. 40(a) it is observed that the force/deflection curve remains linear up until a deflection of roughly 5 mm. A further semi-linear region extends up to a deflection of roughly 7mm, after which the curve flattens out. Using the flexural strain formula we can determine the strain on the surface of the strip using the following equation [2]:

$$\epsilon_{\mathrm{f}} = \frac{6t\delta}{L^2} \tag{31}$$

Combining equation 30 and 31 allows us to solve for the radius of curvature $\rho$.

$$\rho = \frac{L^2}{12\delta} \tag{32}$$

This results in an end to the linear regime at roughly $\rho_{\mathrm{Llimit}} = 26.7\,\mathrm{mm}$, and and end to the semi-linear regime at roughly $\rho_{\mathrm{NLstart}} = 19\,\mathrm{mm}$.

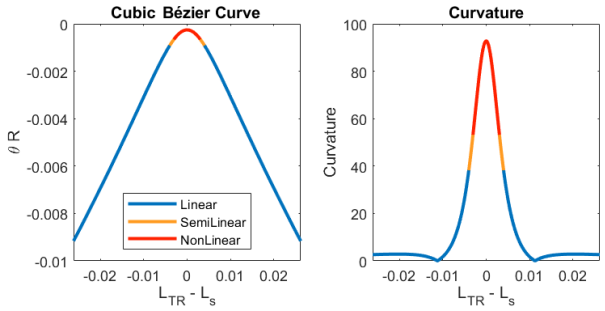


Fig. 41. Cubic Bezier predictions for the transition region (left), and the curvature (right).

Since a predictive model is preferred, a method to predict the radius of curvature along the transition region is required. This is achieved by using the bezier transition region prediction model discussed in Appendix B. For every point along the transition region the radius of curvature is calculated, if this value exceeds either the first or the second region criterion a line is plotted warning the user that the edge has entered a nonlinear elastic region. The warning being triggered as soon as a point in the edge enters nonlinear behaviour, does not immediately invalidate the prediction, as most of the deflection might still happen in the linear regime.

Evaluating $\rho_{\min}$ for a combination of $\alpha$ inputs between 1 and 20 rad/m and $R$ inputs between 2 and 20 mm it is found that only the rate of twist has an influence of $\rho_{\min}$. This appears to follow from the radius being both a factor to the width as well as the height of the bezier curve, thus largely canceling out. It can therefore be determined that using $\rho_{\mathrm{Llimit}}$ and $\rho_{\mathrm{NLstart}}$ the linear elastic response is completely valid until $\alpha = 10\,\mathrm{rad/m}$, and the nonlinearly elastic response starts at $\alpha = 14\,\mathrm{rad/m}$. These values are much lower than those used in the paper. Therefore, further research should be performed into the effect of nonlinear elastic behaviour in the helicoidal shell.

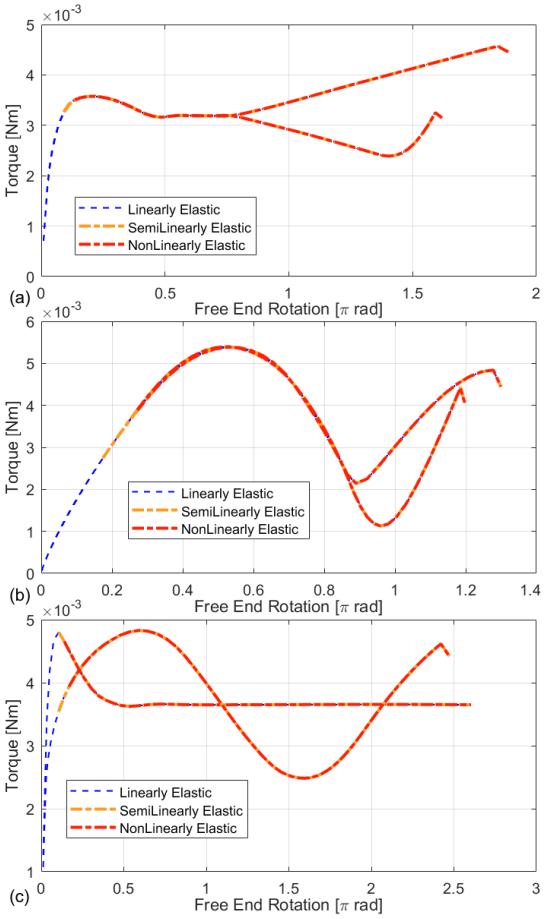


Fig. 42. The elastic regimes at the edge shown for each designed curve

### References


[1] James M. Gere. *Mechanics of Materials, SI Edition*. 7th. Stamford, CT: Cengage Learning, 2009. ISBN: 978-0-495-55834-9.

[2] Z. Jia et al. "An experimental investigation of the temperature effect on the mechanics of carbon fiber reinforced polymer composites". In: *Composites Science and Technology* 154 (2018), pp. 53–63. DOI: 10.1016/j.compscitech.2017.11.015.

### H. Design Goal for the Interface

One of the goals of the thesis is to create an easy to use design software, that allows for quick iteration of variable torque-twist Helicoids. Secondarily, this software also includes the research interfaces made to determine the variables of the determined formula.

The software was intended to have two main design modes, one where a torque-twist curve could be designed directly. Once designed, the program would back-solve it to a geometry that would generate that torque twist profile. This idea became unfeasible for two reasons. The first being that the analytical solution can not be resolved for Torque as the variable. The second is that this method requires both the x and y axis to be relatively accurate. Currently the x-axis requires a correction factor as the Saint-Venant stiffness method isn't accurate enough.

Instead the rate of twist $\alpha$ is used to indirectly design the torque-twist curve. This is possible due to the similarity between the shape of the twist angle and that of the resulting torque. For this purpose a design interface is written, in which the shape of the rate of twist curve can be altered using the control points of a B-spline. Initial rough design can be done by dragging points with the cursor, whilst fine tuning can be achieved by setting their exact coordinates. A live plotted line shows the current prediction. Once the user is satisfied with the predicted curve, it can be committed to the Predictions Window using a button. The software allows for the rescaling of the length, radius and shell thickness. After the FEM simulation the resulting line can be used as a guide to alter the geometry slightly in order to achieve the desired torque-twist profile. It also allows the user to correct the Saint-Venant such that it fits the FEM result curve.

Once a satisfactory curve is achieved it can be exported as an .IGES file to integrate it into a pre-made SolidWorks model. The geometry and data collected from the FEM calculations can also be saved, this allows for curves to be loaded in subsequent sessions.

A further feature is the history interface, this uses the history data collected from the FEM to plot a few things. It also allows for the fitting of the Gauss window, as well as the Bezier transition region curve.

### I. Using the Design Interface

As the previous section treated the general idea behind the design interface, it did not dive deeply into each and every part. This section, therefore, introduces some further functions of the interface and expands on some of the functions already mentioned.

Two versions of the program exist: The version provided with this thesis is a stand alone version that omits the FEM software written and adapted by Nagy et al [1] and Radaelli [2]. A second version, made for further Helicoidal shell research, does include these features.

#### 1) Installing the program

The files provided allow for the program to be loaded in two ways. The first being as an app inside of MATLAB itself called: "Wokkel Design Interface.mlappinstall". The second is as a .exe file called: "Wokkel_design_Interface.exe". For the .exe option the correct version of the MATLAB runtime executible should be installed 2022b(9.13) which can be found on the MATLAB website under MATLAB Compiler. This software is free and meant to allow for MATLAB files to run if no full installation is present.

#### 2) Setting up a curve

When first booting the interface the user will be shown the Mode Selection Window, here the non-choice can be made between the geometry and torque design modes. The latter of which doesn't exist yet. After the user has chosen the geometry design option a second choice can be made, between setting up a constant torque curve and manually placing points. Choosing the Constant torque curve will open a window where the main parameters can be set. This will generate a constant rate of twist curve with a nucleation region that spans a third of the spine length. If the user choses to place the control points manually, a window will be opened where the points can be placed individually. Of these, the first point placed will always be moved to the right end of the curve, thus only its height can be controlled. A third option is to load a previously saved curve, these can be found in the folder "SavedFiles" within the project folder.

#### 3) Controlling the Curve

Once a curve has been set up, the red control points can be dragged into position. The control point control the green rate of twist curve using a B-spline. This curve is used to calculate the light blue torque shape in the design window and live prediction in the Predictions Window. The torque shape is a dimensionless visualisation of the resulting Torque curve, useful in as far as it visualises what part of the rate of twist curve is responsible for the corresponding part in the torque prediction curve. If more precise control is desired, than dragging can achieve, the "●" button, can be pressed. This button will open the list of the coordinates of all the control points. There are two more limited control points:

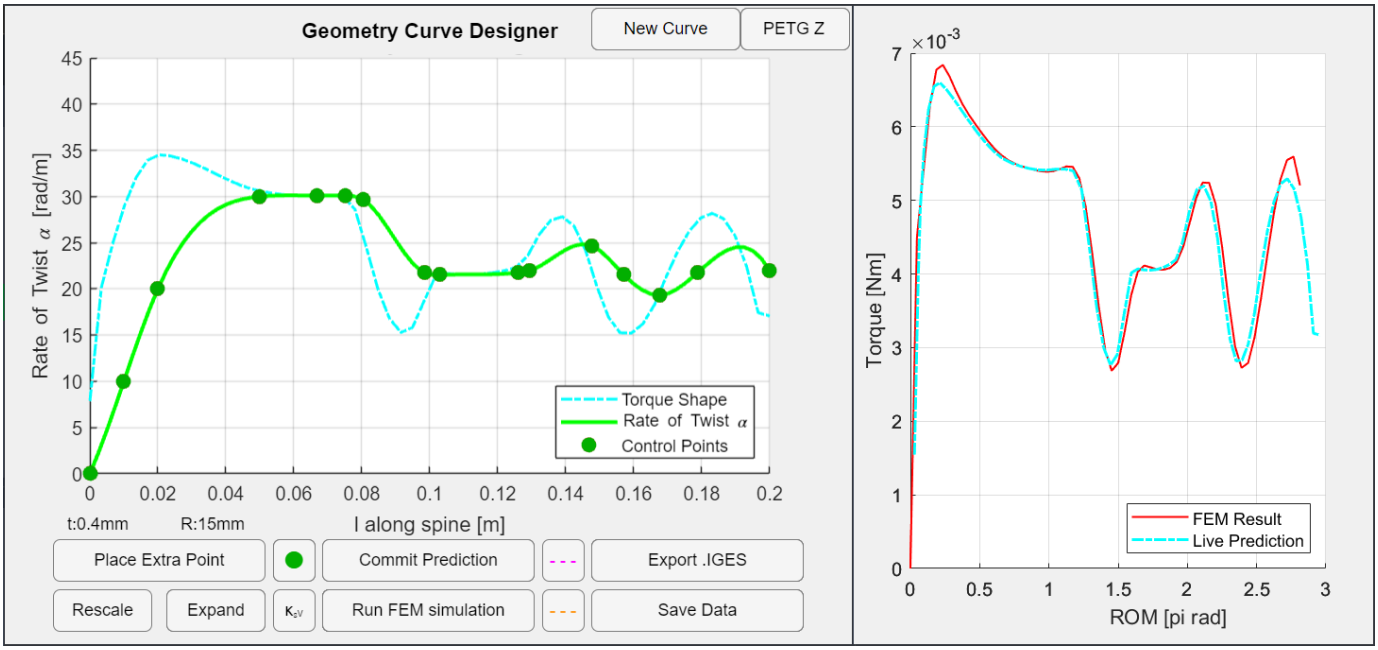


Fig. 43. Design Software Interface used to design torque-twist curves. The example here is that of an MRTTT curve. On the left is the design interface, where the red control points can be dragged in order to affect the rate of twist spline. A live Torque shape will be shown in the same window, as well as in the window on the right. Here one can also plot guide curves to follow. Once the predicted curve is close to the desired one, a FEM simulation can be used to verify the Torque-Twist curve, after which manual iterations can be performed to get the FEM result to where it is desired. The design interface will be further discussed in Appendix. H.

The control point in the origin however cannot be moved, nor can the x-position of the right-most point be changed by dragging it. If a point is dragged it can be moved anywhere in the figure as the order of the control points in the code rearranges based on their spinal axis coordinate. If more control points are desired, the button 'Place Extra Point" can be pressed, this will open the same point placing interface as described earlier. Control points, once added, can not be removed.

*4) Rescaling and Expanding*

The button 'Rescale' allows the user to change the design parameters of the curve. The window dimension can be altered, and the control points will scale accordingly. In the resulting window the amount of discrete slices can be set as well, both for the prediction as well as for the FEM. All inputs in this window allow for basic mathematical operations. The button 'Expand' only refers to the window dimensions. Therefore, if the window is expanded along the spinal axis, it will only change the spinal axis coordinate of the right-most point. This allows for extra working space if required. If an decrease in the window width leaves certain control points outside the window, they can be moved back in frame using the 'list' button. This property can be used when a constant curve is made, as it can change the percentage of the curve dedicated to the nucleation region, by a combination of Expanding and Rescaling the curve.

*5) Guidelines*

If a specific curve is desired that needs to be adhered to perfectly guidelines can be plotted. These can be dimensioned using the Guideline Window shown in Fig. 44, which is opened by pressing the magenta "---" button. In this window two preprogrammed lines are available: a straight line and a sinus. Both curves can be set between two points, where the sinusoidal curve is simply added to the straight line. An example using the same coordinates for the two endpoints is shown in Fig. 45, which are the result of the inputs given in Fig. 44. If a specific curve is desired, it can be programmed in the code line, using the given functions. The line will be plotted between X1 and X2, in a 100 steps. The input should either be a single value, in which case, it will become a line with a constant height, or an array with a 100 entries. The function symbol Y(100) will become Y(100) if the function is invalid, or Y(100) if the amount of array entries is neither 1 nor 100.

*6) Saint Venant Stiffness correction*

The "$K_{SV}$" button allows the user to adjust the Saint-Venant Stiffness after an initial FEM verification result has deemed it necessary. In this window one can also get the stiffness numerically calculated, but as this solution won't take the transition region into account it is usually too compliant for the prediction.

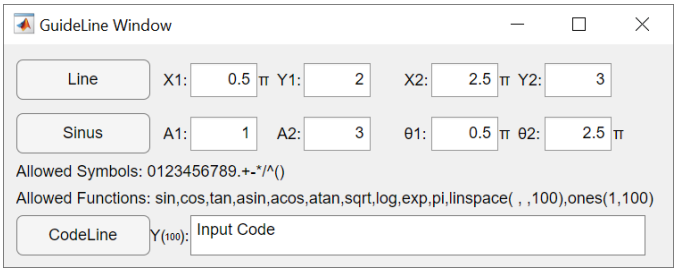


Fig. 44. Guideline Window, its resulting line and sine curve are shown in Fig. 45, where the inputs are also visualised.

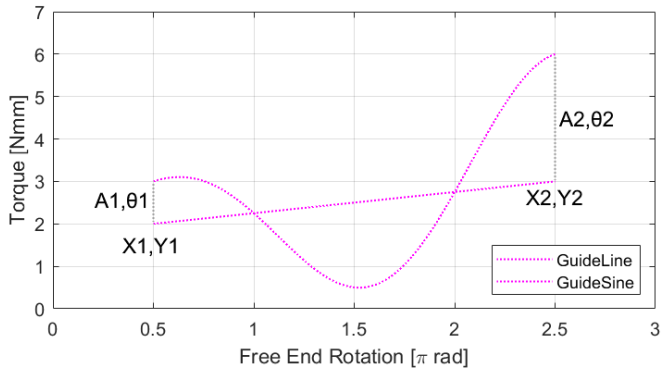


Fig. 45. Resulting guidelines of the Fig. 44. Both curves use the same x and y coordinates, but the sinus ads extra inputs for the start/end amplitude and angle.

### 7) Material Selection

In the top right there is a button that displays the currently chosen material. Once pressed it will open a window where the saved materials are displayed. Using the input field the user can choose a number from the list. Once selected the material properties are shown on underneath. These properties can be edited by pressing the ”Edit” button. The user can also choose to add a new material. The input fields in these windows allow for basic math inputs. The Material can be chosen as soon as the program starts, this means that any loaded file will have the height of its saved FEM curve adapted to the chosen material.

### 8) Determining Elastic Regime

In order to determine the elastic regime in the edge, the orange ’---’ button can be pressed. This will, using the bezier transition region shape prediction discussed in Appendix E, plot either a orange or a red dashed line. The orange dashed line denotes that some part of the edge transition region exceeds th linear behaviour. The red dashed line denotes that it has entered the nonlinearly elastic region. For most curves designed, using PETG, the linearly elastic curve will be exceeded.

Pressing the orange ’---’ button will secondarily open a window that allows the user to inspect the bezier prediction

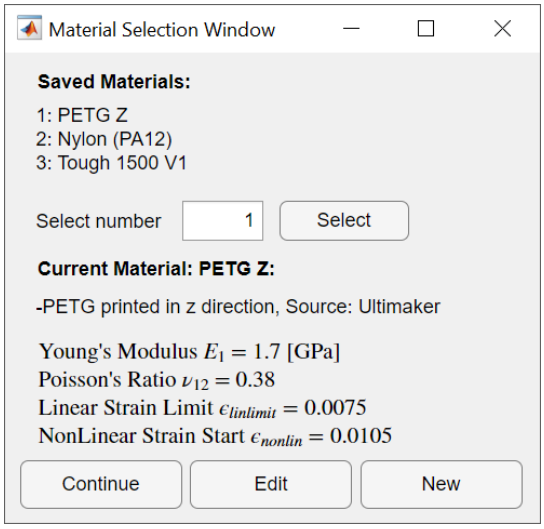


Fig. 46. The Material Selection Window

of the elastic regimes of a transition region, for a specific point along the spinal axis.

### 9) FEM verification

If the version with an included FEM program is used, the predicted curve can be verified using the ”Run Fem Simulation” button. This will start the FEM simulation in the amount of FEM steps defined in the rescale window. Each iteration it will plot a figure that shows the current 3D configuration, as well as FEM simulation progress.

### 10) History Interface

If the version with the FEM This version will also include the History Interface button called ”Hst”. This will open a second interface where the saved geometry configuration can be observed for every FEM step, and slice coordinate. It allows for observation of the total in-slice deflection angle $\Gamma$, the local in-slice deflection angle $\gamma$ and the in-slice deflection. It also allows the user to plot the cubic bezier prediction over the orientation plot, as well as use the $\Gamma$ plot to fit a Gauss transition region prediction (this was investigated until the cubic Bezier method proved more effective).

## References


[1] Attila P. Nagy, Samuel T. IJsselmuiden, and Mostafa M. Abdalla. “Isogeometric design of anisotropic shells: Optimal form and material distribution”. In: *Computer Methods in Applied Mechanics and Engineering* 264 (Sept. 2013), pp. 145–162. ISSN: 00457825. DOI: 10.1016/j.cma.2013.05.019.

[2] Giuseppe Radaelli. “Reverse-twisting of helicoidal shells to obtain neutrally stable linkage mechanisms”. In: *International Journal of Mechanical Sciences* 202-203 (2021). ISSN: 00207403. DOI: 10.1016/j.ijmecsci.2021.106532.

*J. Making a SolidWorks Model*

Open the ”Base SolidWorks Model” inside the folder. Open the Equations tab and change the Radius ”R” and Flange Thickness ”T” to the desired values.Update the imported file. At this point 6 features should be broken, these can be reapplied in the following order:

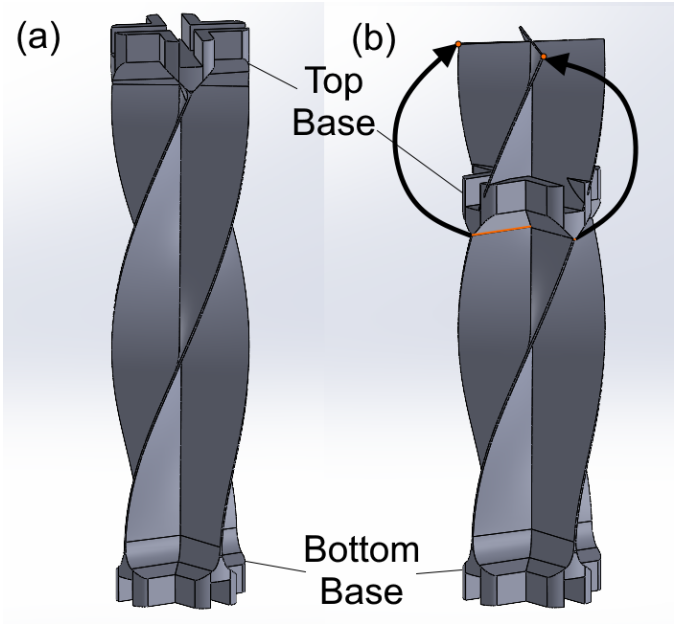


Fig. 47. (a) The finished SolidWorks model. (b) The SolidWorks model after a new .IGES file has been loaded. Both the top and bottom base will need to be realigned, although the bottom should already be in the final position.

”Body-Move/Copy1 Bottom Base” Replace the broken connections with new ones. The parts to connect are shown in Fig. 47, where the vertex of the base is paired with the corner of the helicoid. For the bottom base it should not matter which corner is chosen, as they are both at the same height coordinate.

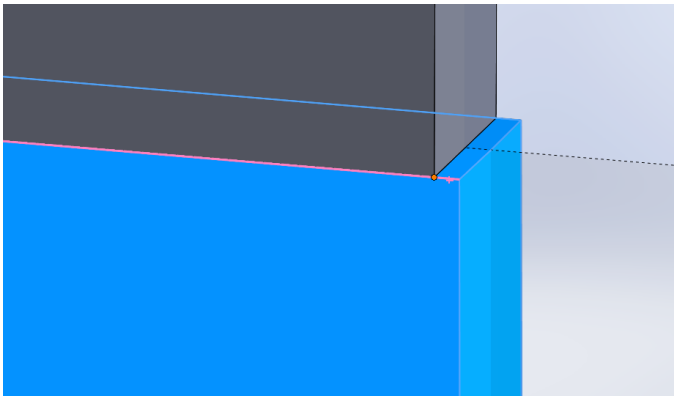

Fig. 48. Fillets shown for the bottom base. The Orange line shows the vertex where the fillet is to be applied. The orange dot shows the corner of the helicoid geometry.

”Body-Move/Copy2 Top Base” Replace the broken connections with new ones. The parts to connect are shown in Fig. 48, where the vertex of the base is paired with the corner of the helicoid. For the Top Base it is important to chose the correct corner. Chose the corner with the lowest height coordinate in order to make sure that there are no gaps between the parts.

”Fillet20 BottomBase Helicoid Connection” For this step to function, it is important that the imported geometry starts with a 0 $\alpha$ region. If that is the case it should suffice to simply reapply the fillet to all 8 sides of the curve as shown in Fig. 49. The fillet might occasionally be applied in the opposite orientation, so make sure that you use the steeper orientation.

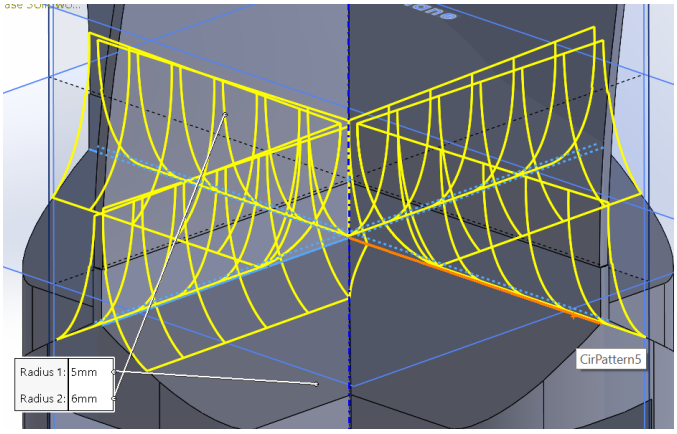


Fig. 49. Fillets shown for the bottom base. Orange line shows the vertex where the fillet is to be applied.

”Chamfer21 TopBase Helicoid Connection Smoothing” This chamfer serves to make the obtuse fillet work. It needs to be applied, a total of 4 times, as shown in Fig. 50.

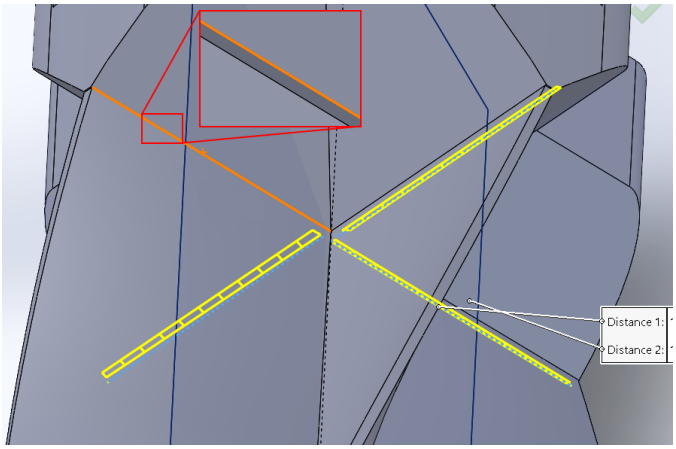


Fig. 50. Chamfers shown for the top base. Orange line shows the vertex where the fillet is to be applied. A zoomed in part shows the two nearly overlapping vertices and which should be used.

”Fillet22 TopBase Helicoid-Chamfer Connection” Fig. 51: The obtuse fillet that connects the helicoid to the chamfer applied in the previous step. It is applied 4 times as shown, here it is important that the correct edge is selected as there are two near overlapping edges, of which only one will result in the desired fillet.

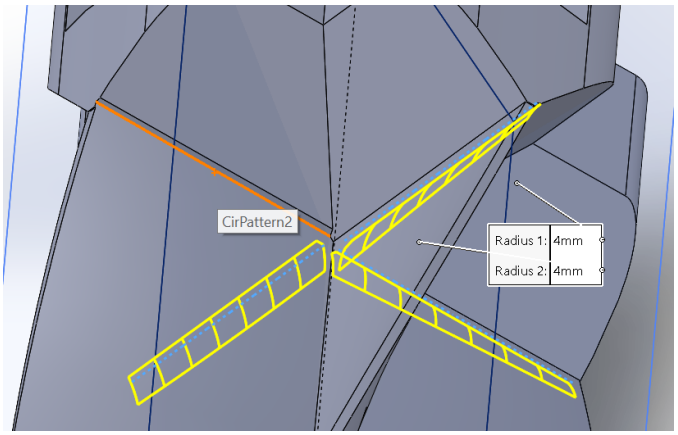


Fig. 51. Fillets shown for the top base. Orange line shows the vertex where the fillet is to be applied.

”Fillet23 TopBase Helicoid Connection” Fig. 52: The fillet that connects the Sharper side of the top base. It can simply be applied a total of 4 times.

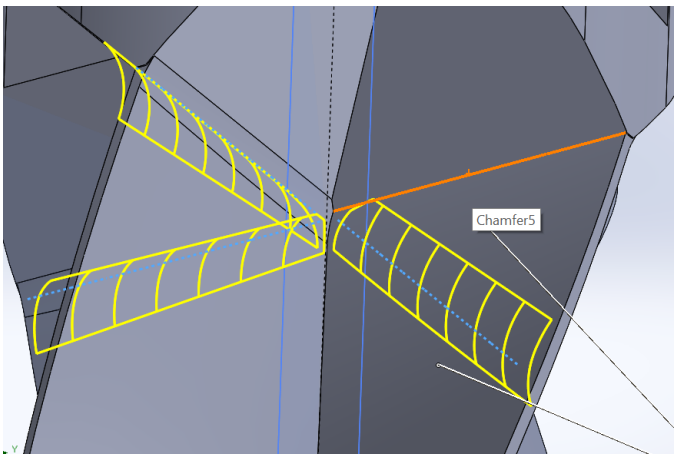


Fig. 52. Fillets shown for the top base. Orange line shows the vertex where the fillet is to be applied.